UNIVERSITÀ DEGLI STUDI DEL PIEMONTE ORIENTALE

Dipartimento di Scienze Della Salute

Master's Degree in Medical Biotechnologies

Mathematical modelling and Sensitivity Analysis of Nurse Macrophage-Driven Erythropoiesis Disruption in Acute Myeloid leukaemia

Supervisor: Prof. Lia Rimondini
Università degli Studi del Piemonte Orientale

Co-supervisor: Dr. Marc Sturrock
Royal College of Surgeons in Ireland (RCSI)

Lia Rimondini

Msturrock

Firmato digitalmente da Lia Rimondini
Data: 06.03.2026 16:50:42 CET
Organizzazione: UNIVERSITA' DEGLI STUDI DEL PIEMONTE ORIENTALE/01943490027

Candidate: Shayan Jalali
Matriculation number: 20057956

Academic Year 2023–2025

Table of Contents

Summary

Rationale

Erythropoiesis occurs within erythroblastic islands (EBIs), specialised bone marrow niches composed of a central nurse macrophage surrounded by differentiating erythroblasts. Nurse macrophages support erythropoiesis by clearing extruded nuclei, recycling iron, and providing cytokine signals that promote erythroid proliferation and maturation. In acute myeloid leukaemia (AML), this microenvironment is disrupted and anaemia is common, yet the mechanisms linking leukaemic remodelling of EBIs to erythropoietic failure remain incompletely understood.

Planning

This study integrates experimental data from murine MLL-AF9 AML models and human xenografts with a mechanistic mathematical model describing dynamic crosstalk between nurse macrophages and erythroblasts under healthy and leukaemic conditions. A system of ordinary differential equations implemented in `R` were used to simulate erythroid population dynamics, cytokine feedback, and AML-associated macrophage dysfunction. Parameter values were informed by experimental measurements and the literature, and Global Sensitivity Analysis (GSA) was applied to identify regulatory processes that most strongly control erythroid output and EBI stability.

Results

Model simulations reproduced experimental erythroid kinetics and indicated that perturbations in macrophage cytokine signalling and iron recycling can substantially suppress erythroid maturation, consistent with in vivo AML bone-marrow observations. GSA identified macrophage-centred regulation as a dominant determinant of system behaviour, highlighting M-CSF signalling, macrophage iron handling, and cytokine-driven control of erythroid proliferation among the most influential mechanisms governing erythropoietic efficiency.

Conclusions

This integrative experimental–computational study provides a quantitative framework for explaining how AML disrupts erythroid niches through macrophage dysfunction. The model nominates macrophage-centred pathways, particularly M-CSF signalling and iron recycling, as tractable therapeutic targets and offers a foundation for testing niche-focused interventions in future experimental and translational studies.

Acknowledgements

I would like to express my deepest gratitude to Dr. Marc Sturrock for his outstanding guidance, constructive feedback, and continued support throughout this thesis. During my Erasmus+ placement at the Royal College of Surgeons in Ireland (RCSI), Dublin, his mentorship was central to shaping both the direction and the quality of this work, and I am sincerely grateful for his patience, insight, and encouragement.

I am also grateful to Prof. Jochen Prehn for his support, valuable discussions, and for fostering a stimulating research environment at RCSI. I thank the RCSI Department of Physiology and Medical Physics for providing an excellent scientific setting throughout my Erasmus+ period.

I would like to thank Dr. Davide Cora (Bioinformatics Laboratory, Department of Translational Medicine, University of Eastern Piedmont Amedeo Avogadro) for his helpful input and thoughtful comments, which improved the clarity and presentation of parts of this thesis.

I sincerely thank my home university, the University of Eastern Piedmont Amedeo Avogadro (UPO), for academic support and coordination throughout my studies. In particular, I am grateful to Prof. Lia Rimondini for her continued encouragement and support.

I also thank Prof. Diego Cotella for his coordination of the Erasmus+ programme and for facilitating the administrative and academic framework that made this placement possible.

This work was carried out within the framework of the Erasmus+ programme and was co-funded by the European Union.

Introduction

1.1 Acute Myeloid Leukaemia and Bone Marrow Microenvironment

Acute myeloid leukaemia (AML) is an aggressive haematological malignancy and a major clinical challenge worldwide[1]. It predominantly affects older adults and is associated with poor prognosis and high relapse rates, even after intensive chemotherapy or allogeneic haematopoietic stem cell transplantation[2–4]. Severe cytopenias are a hallmark of AML, and anaemia is nearly universal, contributing to morbidity, transfusion dependence, and reduced survival[5,6]. Despite decades of research, the mechanisms driving AML-associated erythropoietic failure remain incompletely understood[7,8]. Although physical crowding by leukaemic blasts can contribute to haematopoietic suppression, increasing evidence indicates that AML actively remodels the bone marrow (BM) microenvironment, disrupting supportive niches required for normal haematopoiesis, including erythropoietic niches maintained by erythroblastic islands and their central nurse macrophages[6,9–11]. AML can also perturb vascular and endosteal niche components through depletion of endosteal vessels and osteoblast-associated signals, alongside broader alterations in haematopoietic niche macrophages[12–14]. In AML, macrophages often acquire leukaemia-supportive characteristics, and patients exhibit expansion of $CD163^{+}CD206^{+}$ M2-like macrophages compared with healthy controls[15–17]. Nurse macrophages within erythroblastic islands (EBIs) are a distinct subset specialised for erythroblast maturation and iron recycling[18,19]. Their loss contributes to, but does not fully explain, AML-associated anaemia, which is also driven by inflammatory cytokine–mediated suppression of erythropoiesis, reduced erythropoietin signalling, and altered systemic iron regulation[20,21].

EBIs are specialised niches composed of a central nurse macrophage surrounded by differentiating erythroblasts[10,22]. Within EBIs, nurse macrophages provide adhesion and signalling cues, clear extruded nuclei from orthochromatic erythroblasts, secrete cytokines and growth factors that support erythroblast survival and maturation, and recycle iron for haemoglobin synthesis[19,23]. EBIs are particularly important during stress erythropoiesis, such as anaemia, when erythroid output must be amplified[11,23]. In AML, collapse of erythropoiesis is accompanied by disruption of macrophage iron handling and accumulation of iron in plasma and ferritin[21,24].

AML can actively remodel EBIs and their nurse macrophages[6]. Imaging and cytometry studies show selective loss of $CD169^{+}$ nurse macrophages in AML-infiltrated marrow, with local remodelling detectable even at low leukaemic burden[6,12]. Functionally, EBIs in AML contain fewer associated erythroblasts and show impaired support for terminal erythroid maturation, and anaemia severity does not correlate linearly with overall marrow infiltration, supporting niche disruption as a dominant driver beyond space competition alone[6,25].

Nurse macrophages depend on macrophage colony-stimulating factor (M-CSF) for survival and function[10,18,26,27], yet erythropoiesis models rarely integrate AML-induced niche disruption or loss of M-CSF signalling into erythroid dynamics. This motivates our focus on M-CSF-dependent macrophage support and its potential contribution to restoring erythropoiesis in the leukaemic marrow environment[8,28].

1.2 Erythropoiesis in the Bone Marrow and Spleen

Erythropoiesis generates red blood cells (RBCs) from haematopoietic stem cell (HSC)-derived progenitors[29]. In adult humans, approximately 2–3 million RBCs are produced every second under steady-state conditions[29–32]. HSCs differentiate through common myeloid and megakaryocyte–erythroid progenitor (MEP) stages to committed erythroid progenitors (BFU-E and CFU-E), which proliferate under erythropoietin (EPO) and stem cell factor (SCF) and mature through erythroblast stages to enucleated reticulocytes and finally erythrocytes[29]. Early erythroblasts proliferate rapidly, whereas late stages exit the cell cycle and undergo haemoglobinisation and enucleation[29].

Efficient erythropoiesis depends on specialised bone marrow niches. Erythroblastic islands (EBIs) organise erythroid cells around a central macrophage that delivers trophic support (including iron), provides growth cues, and clears extruded nuclei, thereby promoting proliferation and terminal differentiation[18,29,33]. Additional niche cells contribute; for example, leptin receptor-positive stromal cells supply SCF required to support erythroid progenitors in the marrow[34,35]. Disruption of niche integrity or growth factor signalling can cause ineffective erythropoiesis and anaemia even when progenitors are present[18,29].

While the bone marrow is the primary site of adult RBC production, the spleen can act as an auxiliary erythropoietic organ during stress erythropoiesis, a demand-driven response to anaemia or hypoxia[36,37]. Although minimal in steady-state adults (particularly in humans), splenic extramedullary erythropoiesis can increase when marrow output is impaired; in AML and other marrow-failing states it may partially compensate for suppressed marrow production and contribute to splenomegaly[36,37]. In stress settings, haematopoietic progenitors can establish erythropoietic niches in the splenic red pulp, supported by resident macrophages[36,38].

This compensatory contribution is represented in mathematical models using a spleen-derived RBC source term ρ_{spleen} upregulated by an anaemia factor A[39]:

$$\text{RBC input from spleen} \;=\; \rho_{\text{spleen}}\,(1 + 2.8\,A)$$

$$\frac{dR}{dt} \;=\; \rho_{\text{spleen}}\,(1 + 2.8\,A) \;+\; \gamma_{\text{OrthoE}\to\text{R}}\,\text{OrthoE} \;-\; \delta_{\text{R}}\,R.$$

Biological relevance and limitations. The spleen term represents *extramedullary erythropoiesis* as a compensatory response during marrow failure and anaemia; in AML it may partially replace suppressed marrow RBC output, as reported in murine and occasional human cases of leukaemic splenomegaly[39,40]. Because quantitative data on spleen-driven erythropoiesis in AML remain limited, this component is implemented as a simplified proxy and should be interpreted as a *phenomenological* representation of stress erythropoiesis rather than a calibrated prediction of splenic output.

1.3 Nurse Macrophages and Erythroblastic Islands in Haematopoiesis

Erythroblastic islands (EBIs), first described by Bessis in 1958, are specialised erythropoietic niches organised around a central *nurse macrophage*, which exhibits a tissue-supportive, M2-like activation state suited to erythroid maturation[10,22,23,41,42].

Two EBI subtypes have been described in bone marrow: immature EBIs located deeper in the parenchyma and enriched for early erythroblasts, and mature EBIs positioned near sinusoids where macrophages interact with late-stage erythroblasts, facilitating orderly maturation and release into circulation[23,41].

Within EBIs, nurse macrophages provide growth cues (e.g. SCF and IL-6), deliver iron (via ferritin, heme, or transferrin) for haemoglobin synthesis, and phagocytose extruded nuclei (pyrenocytes), limiting inflammatory debris and enabling recycling of cellular components; under stress (anaemia or hypoxia), EBIs expand and macrophage support intensifies to increase red cell output[10,23,41,42].

The importance of macrophage–erythroid interactions is reflected in disease: in β-thalassaemia and polycythaemia vera (PV), abnormal EBI function contributes to pathology[43,44]. In a JAK2^{V617F} PV model, macrophage depletion reduced excessive erythropoiesis, whereas enhancing macrophage activity improved recovery from anaemia[11,44].

Mathematical models increasingly represent EBIs as dynamic functional units, emphasising cell–cell communication and cytokine networks, particularly macrophage colony-stimulating factor (M-CSF), as regulators of nurse macrophage survival and erythroid support[10,45–47].

1.4 AML Impact on Erythropoiesis and EBIs

Acute myeloid leukaemia (AML) infiltration profoundly disrupts erythropoiesis[6,48]. Anaemia is nearly universal, even at low marrow blast percentages, indicating mechanisms beyond physical replacement of erythroid precursors[6]. Experimental studies further show that AML impairs the erythroblastic island (EBI) niche and can collapse the macrophage–erythroblast architecture required for terminal maturation[20].

In a murine MLL-AF9 AML model, leukaemic expansion caused early depletion of late-stage erythroblasts (polychromatic and orthochromatic stages), reduced numbers of intact EBIs, and impaired erythroblast proliferation, even at low leukaemic burden[6]. Phenotypically defined nurse macrophages were significantly diminished in both murine and human AML bone marrow, whereas other leukaemias such as T-ALL did not show the same niche-specific defect[6].

Reduced availability of macrophage colony-stimulating factor (M-CSF; CSF-1) in leukaemic marrow appears to contribute to nurse macrophage attrition; supplementation in AML-bearing mice partially rescued nurse macrophages and was associated with improved erythropoiesis[47]. These findings support a model in which AML remodelling destabilises macrophage survival, promoting EBI collapse and ineffective erythropoiesis.

AML also perturbs systemic iron metabolism. Clinical profiling identified an iron-loading phenotype characterised by elevated ferritin, low transferrin, and paradoxically high transferrin saturation (TSAT), contrasting with anaemia of chronic disease[21]. In AML models, erythroblast depletion reduces incorporation of iron into haemoglobin, leading to accumulation of plasma iron and ferritin and increased TSAT; this is accompanied by elevated hepcidin and evidence of iron sequestration by AML blasts (increased CD71 and altered ferroportin), together shifting iron distribution toward plasma and leukaemic cells[21]. Notably, systemic iron overload (e.g. iron dextran or *Hfe*$^{-/-}$ mice) slowed AML progression, and higher TSAT at diagnosis was associated with improved overall survival, suggesting

that AML-associated erythropoietic shutdown and iron redistribution can create a milieu less permissive for leukaemic expansion[21].

1.5 Bone Marrow Niche Remodelling in AML

AML not only suppresses erythropoiesis but broadly remodels the bone marrow (BM) microenvironment, disrupting supportive niches required for normal haematopoiesis[7,48–51]. A prominent change is the polarisation and expansion of tumour-associated macrophages (TAMs): AML blasts secrete factors including Arginase II and cytokines that promote an M2-like phenotype[15,52]. Single-cell profiling of AML patient marrow has identified macrophage subpopulations skewed toward immunosuppressive, pro-tumoural states[53]. Functionally, AML-conditioned macrophages exhibit reduced phagocytosis of blasts, and bone marrow stromal cells can transfer functional mitochondria to leukaemia cells, enhancing metabolic fitness and chemotherapy resistance[54,55]. In experimental models, M2-like macrophages accelerate AML progression, whereas eliminating or reprogramming these macrophages can impair leukaemia growth[54,55].

AML also alters stromal and structural niche components. Mesenchymal stromal cells (MSCs) can measurably shift towards AML-supportive states, including senescence; for example, AML induces $p16^{INK4a}$-dependent senescence in bone marrow fibroblasts with a secretory profile that promotes leukaemic cell survival[56–58]. Osteoblast-associated endosteal niche signals may be decreased or functionally impaired, reducing support for normal HSCs and enabling leukaemic cells to dominate endosteal niches[51]. Endothelial cells may also be co-opted: AML can stimulate angiogenesis and exploit vascular niches for leukaemic stem cell (LSC) localisation, partly via CXCR4–CXCL12 interactions[12,59–62]. As AML blasts often overexpress CXCR4, blockade of this axis can mobilise leukaemic cells from CXCL12-rich protective niches into circulation and increase chemosensitivity, an approach under clinical evaluation[49].

Bone marrow adipocytes are also altered in AML. High leukaemic burden is associated with reduced adipocyte content, and AML-derived signals can inhibit adipogenesis, with potential consequences for normal haematopoiesis and niche metabolism[63]. Consistent with a functional role, boosting BM adipogenesis using a PPAR-γ agonist suppressed AML growth in mice while promoting recovery of healthy erythropoiesis[63]. These niche interactions motivate therapeutic approaches that target the microenvironment (e.g. CXCR4 inhibition or macrophage-directed strategies) alongside leukaemia-directed therapy[61,64,65].

To address this, the present study combines experimental data from murine MLL-AF9 AML models and xenograft systems with a computational framework that simulates erythroid–macrophage interactions within erythroblastic islands, with sensitivity analysis used to identify parameters that most strongly govern erythroid output under leukaemic perturbation.

1.6 Mathematical Modelling of Haematopoiesis and Leukaemia

Mathematical modelling provides a quantitative framework to integrate experimental observations and test hypotheses about multi-cellular regulation in haematopoiesis and

leukaemia[66]. Early erythropoiesis models (1960s) used linear compartmental structures to represent progenitor maturation[67], and subsequent work incorporated feedback control, particularly erythropoietin (EPO) regulation in response to hypoxia[68]. A landmark series by Loeffler and colleagues developed comprehensive models of murine and rat erythropoiesis with explicit EPO-driven feedback and distinct bone marrow versus splenic contributions, highlighting increased splenic output during strong erythropoietic stimulation[39,69–71].

As niche biology became better defined, models increasingly incorporated spatial organisation and cell–cell interactions within the bone marrow microenvironment[66]. Erythroblastic islands (EBIs), in which erythroid progenitors proliferate and differentiate in close association with nurse macrophages, were integrated into several frameworks that emphasised local communication and cytokine regulation, including macrophage colony-stimulating factor (M-CSF) as a determinant of nurse macrophage survival and erythroid support[10,18,41,45,46].

Leukaemia modelling has similarly evolved from generic growth models[72–74] to AML stem cell-focused frameworks capturing self-renewal, clonal dynamics, and regulatory feedback[75–78]. Competition models explored interactions between healthy and leukaemic stem cells within the niche, showing that small differences in self-renewal can drive clonal dominance[66,79], and feedback mechanisms can modulate coexistence versus dominance[80,81]. ODE models with leukaemic stem cell (LSC) and blast compartments have also been used to represent treatment via drug-induced death or differentiation terms and to explore remission, relapse, and resistance dynamics[82,83].

Recent efforts increasingly integrate high-dimensional data (e.g. single-cell and lineage-tracing) to inform population dynamics and lineage fate decisions[84–87]. Despite these advances, a critical gap persists: existing models do not fully capture the coupled interplay between AML-driven niche disruption, erythropoietic dynamics, and M-CSF-dependent nurse macrophage support within EBIs[10,66]. This motivates the integrated modelling framework developed in this thesis.

Objective of the Thesis

The overall aim of this thesis is to determine how acute myeloid leukaemia (AML) perturbs normal erythropoiesis and to develop an integrative framework for understanding, and potentially mitigating, these effects. The specific objectives are:

1. **Characterise the dynamics of erythropoiesis** in both the bone marrow and spleen under healthy conditions and during AML-associated stress. This includes examining how AML infiltrates and remodels the bone marrow microenvironment and how compensatory splenic erythropoiesis is activated during anaemia or marrow failure[33,36,38].

2. **Develop and refine a mathematical model** of erythropoiesis that integrates bone marrow and splenic contributions. The model incorporates key regulatory pathways (e.g., erythropoietin response, erythroblastic island and nurse macrophage interactions, and M-CSF regulation) to simulate both steady-state and stress erythropoiesis. This enables quantification of the contribution of extramedullary (splenic) red blood cell (RBC) production during AML progression.

3. **Apply the integrative model** to interpret experimental and clinical data and to derive therapeutic insight. By combining computational simulations with patient data and experimental observations, the thesis aims to identify how interventions (such as cytokine-based modulation of the macrophage niche via M-CSF, or spleen-relevant strategies) might restore effective erythropoiesis or alleviate anaemia in AML[18,88].

Materials and Methods

3.1 Experimental Phase

3.1.1 Experimental Models and Data Sources

Experimental data were generated using syngeneic MLL-AF9 AML mouse models and human AML xenotransplantation in NSGS mice, under EU Directive 2010/63/EU–compliant protocols (i3S Animal Ethics Committee, DD_2019_15)[89–91]. Flow cytometry and imaging flow cytometry were performed as previously described[10,20,89,92], with antibody panels and acquisition settings reported in the supplementary information. These datasets provided quantitative measurements of haematopoietic progenitors, erythroblastic islands (EBIs), and nurse macrophages for model calibration and validation.

3.1.2 Experimental Models: Mice and Human Xenografts

Two *in vivo* models were used to study erythropoiesis and its disruption by acute myeloid leukaemia (AML).

Syngeneic MLL-AF9 AML mouse model. C57BL/6 mice (6–12 weeks old) were maintained under specific pathogen-free conditions. AML was induced by transplantation of syngeneic leukaemic blasts into immunocompetent recipients without conditioning, as previously described. Leukaemia burden and erythropoiesis were monitored at defined disease stages[93].

Human AML xenograft model. NOD/SCID/IL2Rγ^{null} (NSGS) mice received sub-lethal irradiation (180 rads) followed by tail vein injection of 2×10^6 human AML cells (OCI-AML-3 or MOLM-13). NSGS mice support human haematopoietic engraftment through human cytokine expression. Disease progression was assessed by monitoring leukaemic engraftment and erythroid populations in bone marrow and spleen until humane endpoints were reached[89,90,94].

All animal experiments complied with EU Directive 2010/63/EU and were approved by the i3S Animal Ethics Committee (protocol DD_2019_15).

3.1.3 Flow Cytometry and Imaging Flow Cytometry

Bone marrow (BM) cells were obtained by flushing femurs and tibias in PBS containing 2% fetal bovine serum (FBS), followed by ammonium chloride lysis and washing. Single-cell suspensions were stained with fluorochrome-conjugated antibodies against erythroid and myeloid surface markers. For erythroid maturation analysis, antibodies included anti-Ter119, CD71, and CD44. For leukaemic and myeloid populations, panels included CD11b, Gr-1, and c-Kit, among others. Acquisition was performed on a BD FACS Canto II and data were analysed using FlowJo software (Tree Star).

BM cell aggregates were obtained by flushing long bones with IMDM supplemented with 2% FBS and Ca^{2+}/Mg^{2+}. Aggregates were fixed, blocked with anti-CD16/32, and stained with PE-Cy5–Ter119, PE–VCAM-1, and PE-Cy7–F4/80. Images were acquired on an Amnis ImageStreamX system (Luminex) and analysed using IDEAS software. Imaging flow cytometry was used to quantify intact erythroblastic islands (EBIs), defined as Ter119$^+$ erythroblasts in close association with F4/80$^+$ central macrophages expressing VCAM-1, enabling assessment of EBI frequency and integrity in healthy and leukaemic BM[41,95,96].

3.1.4 EBI Isolation and RNA-Seq Data Acquisition

EBIs were enriched from bone marrow using a discontinuous BSA gradient (3% bottom, 1.5% top) to separate intact cell clusters from single cells and debris, as described previously[10,20,88,97]. Aggregates were collected from the interphase and stained with fluorochrome-conjugated antibodies. Nurse macrophages were identified as F4/80$^+$CD169$^+$VCAM-1$^+$ cells and sorted on a BD FACS Aria II cell sorter[10,20,95,97].

Total RNA was extracted using the *RNeasy Plus Micro Kit* (Qiagen), and RNA integrity was assessed with an *Agilent Bioanalyzer* (RIN $>$ 7.0). Libraries were prepared with the *Ion AmpliSeq Mouse Gene Expression Kit* and sequenced on the *Ion Torrent Proton* platform (3–5 million reads per sample). Reads were quality-checked using *FastQC* and processed using the Ion Torrent Suite software for alignment and quantification. Differential expression analysis was performed in *R* (v3.5.1) using *DESeq2*, with $\log_2$ fold changes and Benjamini–Hochberg adjusted p-values reported. Visualisation and exploratory analyses (PCA, volcano plots, and clustering heatmaps) were generated using *ggplot2* and *pheatmap* in *R* within a Linux-based reproducible workflow.

3.1.5 M-CSF Treatment Protocol and Reagents

Recombinant murine macrophage colony-stimulating factor (M-CSF) (Peprotech, cat. no. 315-02) was diluted in sterile PBS and administered intravenously to MLL-AF9 AML-bearing mice at 10 μg per mouse in 150 μL on days 16, 18, and 20 post-transplantation[46,98,99]. Control animals received PBS only. Mice were euthanised on day 21 for bone marrow and spleen analysis. Treatment efficacy was evaluated using nurse macrophage frequency (F4/80$^+$CD169$^+$VCAM-1$^+$), erythroblastic island integrity, and erythroid maturation profiles, including assessment of immunomodulatory effects under healthy and leukaemic conditions[95,96].

3.2 Mathematical Modelling Framework

This section introduces the ordinary differential equation (ODE) model developed to describe how acute myeloid leukaemia (AML) disrupts erythropoiesis by altering haematopoietic differentiation, erythroblastic islands (EBIs) and nurse macrophages, and cytokine support (including M-CSF)[39,41,45,100]. The framework links experimental observations to a computational system that can be simulated and calibrated under varying AML conditions, enabling mechanistic investigation of niche-driven erythropoietic failure and *in silico* testing of interventions such as M-CSF supplementation.

3.2.1 Experimental Data Used for Model Validation

Quantitative *in vivo* datasets were used to validate the mathematical model against experimental measurements:

(i) **Erythroblast population dynamics.** Flow cytometry quantification of erythroid maturation stages (ProE, BasoE, PolyE, OrthoE) across defined stages of AML infiltration in bone marrow and spleen.

(ii) **Nurse macrophage and erythroblastic island (EBI) quantification.** Imaging flow cytometry quantification of intact EBIs and their central nurse

macrophages (F4/80$^+$CD169$^+$VCAM-1$^+$)[10,20,95,97]. These data were used to validate niche-dependent differentiation parameters.

(iii) **Proliferation within erythroid subsets.** Ki-67 staining was used to estimate cycling fractions within ProE and BasoE subsets for comparison with modelled proliferation terms.

(iv) **Response to M-CSF therapy.** Changes in nurse macrophage frequency, EBI integrity, and erythroid recovery following recombinant M-CSF administration in AML-bearing mice were used to test model predictions[46,101].

(v) **Transcriptomic profiles of nurse macrophages.** RNA-seq profiles of sorted F4/80$^+$CD169$^+$VCAM-1$^+$ nurse macrophages under healthy and leukaemic conditions were used to evaluate inferred regulatory interactions, including cytokines and adhesion-related genes[20,41].

Together, these datasets constrained the model using cellular, functional, therapeutic, and transcriptomic readouts.

3.2.2 Computational Model Structure and Equations

We developed a compartmental ODE model to describe erythropoietic disruption in acute myeloid leukaemia (AML), capturing erythroid maturation, erythroblastic island (EBI) support by nurse macrophages, and AML-driven niche suppression via reduced M-CSF availability[11,41,45].

State variables represent haematopoietic stem and progenitor cells (HSC/MPP), committed erythroid progenitors (ProE), basophilic erythroblasts (BasoE), polychromatic erythroblasts (PolyE), orthochromatic erythroblasts (OrthoE), and mature red blood cells (R). Nurse macrophages (N) were included as an essential niche component for EBI integrity, and AML blasts (A) were modelled as an expanding population that disrupts erythropoiesis.

Transitions between erythroid stages were governed by differentiation rates γ_i, while self-renewal and proliferation were represented by rates ρ_i with logistic constraints to reflect limited niche capacity. Terminal maturation of OrthoE into circulating RBCs was modelled explicitly, with RBC clearance represented by a removal rate δ_{R}.

EBI support was implemented by allowing nurse macrophage abundance to modulate key erythroid differentiation and proliferation terms[10,41,95]. Nurse macrophage maintenance depended on M-CSF, and AML burden was modelled to increase nurse macrophage loss through an AML-dependent term $\delta_N(A)$, consistent with the observed collapse of EBIs in leukaemic marrow[93].

To represent extramedullary compensation, a spleen-derived RBC source term $\rho_{\mathrm{spleen}}(1 + 2.8\,\mathcal{A})$ was added to the RBC equation, where $\mathcal{A}$ denotes an anaemia-driven feedback factor. This enabled stress erythropoiesis in the spleen to be modelled alongside medullary erythropoiesis[36,38,39,102,103].

Parameters were initialised from literature and refined by calibration against the experimental datasets described in Section 2.2.1[39,100].

3.2.2.1 Overview of the Erythropoiesis Model

The model tracks 13 biological populations and molecular factors, grouped into stem/progenitor compartments, erythroid differentiation stages, niche-supportive cells, leukaemic cells, and a regulatory cytokine. The stem and progenitor compartments include haematopoietic stem cells (LKS), common myeloid progenitors (CMP), and megakaryocyte–erythroid progenitors (MEP)[104,105]. Erythroid differentiation is represented by proerythroblasts (ProE), basophilic erythroblasts (BasoE), polychromatic erythroblasts (PolyE), and orthochromatic erythroblasts (OrthoE), with terminal output captured as circulating red blood cells (R). Niche support is represented by nurse macrophages (Nurse) and erythroblastic islands (EBI), which are required for erythroblast survival and differentiation[10,20,45]. The leukaemic population is modelled as AML blasts (A), representing MLL-AF9 cells that expand within the bone marrow niche and compete for limited resources[12,14,51]. Regulation is represented by macrophage colony-stimulating factor (M-CSF), which is required for nurse macrophage maintenance and EBI integrity and is reduced in AML[20,46,51].

Bone marrow capacity and competition factor. A finite bone marrow carrying capacity was imposed ($K = 1$) to represent physical and resource constraints within the marrow niche[81,106,107]. Proliferation of expanding populations was scaled by a competition factor (CF):

$$\mathrm{CF} = 1 - \frac{\mathrm{LKS} + \mathrm{CMP} + \mathrm{MEP} + \mathrm{ProE} + \mathrm{BasoE} + \mathrm{PolyE} + \mathrm{OrthoE} + \mathrm{EBI} + \mathrm{Nurse} + A}{K}.$$

Setting $K = 1$ normalises all state variables to fractions of total marrow capacity. The CF term therefore reduces proliferation as the niche becomes crowded, providing a simple representation of competition for limited space and support factors during AML expansion[12,14,51,81,106–108].

Together, these components define a mechanistic ODE system for erythroid dynamics in both healthy and leukaemic conditions. The next step is computational implementation and calibration, described below.

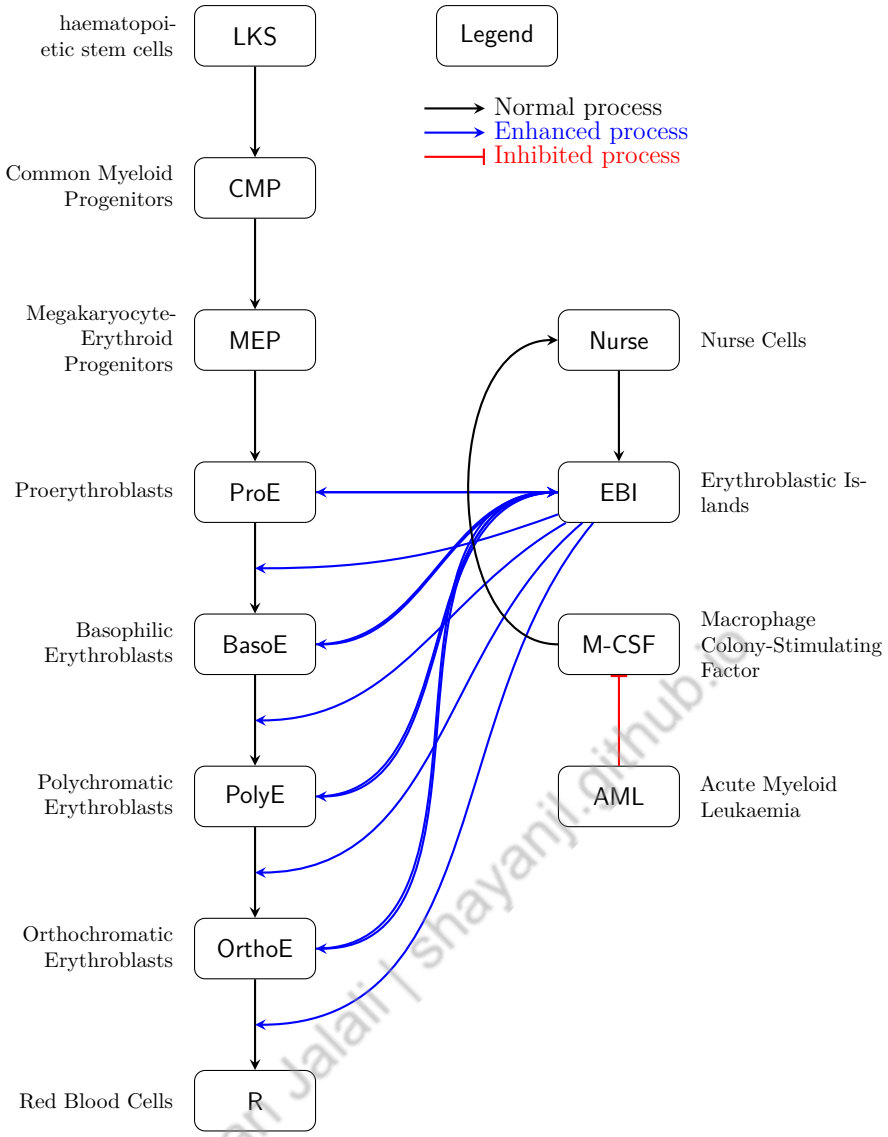

Figure 3.1: The schematic diagram illustrates a simplified view of a comprehensive mathematical model of erythropoiesis and its disruption by acute myeloid leukaemia (AML). Inside each node, the model variable names are displayed with the full variable name outside. The model captures the hierarchical differentiation pathway from haematopoietic stem cells (LKS) through various progenitor stages to mature red blood cells, whilst incorporating the crucial supportive microenvironment of erythroblastic islands (EBIs). The model represents a complex dynamical system with bidirectional interactions between erythroid precursors and EBIs, where nurse cells (central macrophages) form the structural core of these islands. These interactions create a positive feedback loop that enhances erythroid differentiation and maturation. The model also incorporates the pathological effects of AML, which disrupts normal erythropoiesis through inhibition of macrophage colony-stimulating factor (M-CSF) required for nurse cell maintenance[10,20,46,95,97]

3.2.2.2 System of Ordinary Differential Equations (ODEs)

Each equation tracks the rate of change of a specific cell population or regulatory factor, covering the full erythropoietic cascade, the niche components, AML burden, and M-CSF dynamics. Proliferation terms are uniformly modulated by the finite bone-marrow carrying

capacity via the competition factor (CF), ensuring that expansion slows as total cellular load approaches capacity[106].

1. Stem and progenitor compartments. The early haematopoietic modules follow a common structure: net proliferation ($\rho_x\, x \cdot \mathrm{CF}$), natural turnover ($-\delta_x\, x$), and differentiation outflow ($-\gamma_{x\to y}\, x$), with precursor influx where appropriate. Concretely,

$$\begin{aligned}
\frac{d\mathrm{LKS}}{dt} &= \rho_{\mathrm{LKS}}\,\mathrm{LKS}\cdot\mathrm{CF} - \delta_{\mathrm{LKS}}\,\mathrm{LKS} - \gamma_{\mathrm{LKS}\to\mathrm{CMP}}\,\mathrm{LKS},\\
\frac{d\mathrm{CMP}}{dt} &= \gamma_{\mathrm{LKS}\to\mathrm{CMP}}\,\mathrm{LKS} + \rho_{\mathrm{CMP}}\,\mathrm{CMP}\cdot\mathrm{CF} - \delta_{\mathrm{CMP}}\,\mathrm{CMP} - \gamma_{\mathrm{CMP}\to\mathrm{MEP}}\,\mathrm{CMP},\\
\frac{d\mathrm{MEP}}{dt} &= \gamma_{\mathrm{CMP}\to\mathrm{MEP}}\,\mathrm{CMP} + \rho_{\mathrm{MEP}}\,\mathrm{MEP}\cdot\mathrm{CF} - \delta_{\mathrm{MEP}}\,\mathrm{MEP} - \gamma_{\mathrm{MEP}\to\mathrm{ProE}}\,\mathrm{MEP}.
\end{aligned}$$

2. Erythroblast stages (EBI-modulated). Erythroblast maturation (ProE → BasoE → PolyE → OrthoE) is explicitly modelled, with both proliferation (ρ) and differentiation (γ) enhanced by erythroblastic islands (EBIs). Specifically, the EBI-modulated terms are:

$$\rho_X \cdot \left(1 + \frac{\beta_{X,\rho}}{K_{\mathrm{EBI}}}\cdot\mathrm{EBI}\right)\cdot X\cdot\mathrm{CF}, \quad \gamma_{X\to Y}\cdot\left(1+\frac{\beta_{X,\gamma}}{K_{\mathrm{EBI}}}\cdot\mathrm{EBI}\right)\cdot X,$$

where X is the current erythroblast stage and Y the subsequent stage.

For example, for ProE:

$$\begin{aligned}
\frac{d\mathrm{ProE}}{dt} = {}& \gamma_{\mathrm{MEP}\to\mathrm{ProE}}\,\mathrm{MEP} + \rho_{\mathrm{ProE}}\left(1+\frac{\beta^{\rho}_{\mathrm{ProE}}}{K_{\mathrm{EBI}}}\,\mathrm{EBI}\right)\mathrm{ProE}\cdot\mathrm{CF} - \delta_{\mathrm{ProE}}\,\mathrm{ProE}\\
& - \gamma_{\mathrm{ProE}\to\mathrm{BasoE}}\left(1+\frac{\beta^{\gamma}_{\mathrm{ProE}}}{K_{\mathrm{EBI}}}\,\mathrm{EBI}\right)\mathrm{ProE}.
\end{aligned}$$

Analogous equations apply to BasoE, PolyE, and OrthoE with their respective $\rho, \delta, \gamma, \beta$ values.

This structure reflects the biological understanding that EBIs act as supportive niches for erythroblasts, accelerating their expansion and maturation. When EBIs are absent (EBI = 0), proliferation and differentiation rates revert to their baseline values (ρ_X, $\gamma_{X\to Y}$)[10,45,95–97]

3. Red blood cells (RBCs) and splenic compensation. The mature red blood cell (RBC) equation describes the dynamics of mature red blood cells (RBCs). It includes three main components: influx from the bone marrow, contribution from the spleen, and natural turnover. Concretely,

$$\frac{dR}{dt} = \rho_{\mathrm{spleen}}\,(1+2.8\,A) + \gamma_{\mathrm{OrthoE}\to\mathrm{R}}\left(1+\frac{\beta^{\gamma}_{\mathrm{OrthoE}}}{K_{\mathrm{EBI}}}\,\mathrm{EBI}\right)\mathrm{OrthoE} - \delta_{\mathrm{R}}\,R.$$

The first term, $\gamma_{\mathrm{OrthoE}\to\mathrm{R}}(1+\frac{\beta_{\mathrm{OrthoE},\gamma}}{K_{\mathrm{EBI}}}\,\mathrm{EBI})\,\mathrm{OrthoE}$, represents the final maturation step where orthochromatic erythroblasts (OrthoE) develop into RBCs, with differentiation

enhanced proportionally by the presence of EBIs, consistent with the mechanism described for earlier erythroblast stages. The second term, $\rho_{\text{spleen}}(1+2.8\,A)$, captures extramedullary erythropoiesis from the spleen, which is assumed to increase under stress induced by AML burden (A)[36,39,109]. Finally, $\delta_{\text{R}}\,R$ represents the natural turnover or clearance of RBCs from circulation.

4. AML cell dynamics. The AML population (A) grows under the shared marrow carrying-capacity constraint through the competition factor (CF). The governing equation is:

$$\frac{dA}{dt} \;=\; \rho_{\text{A}}\,A\cdot\text{CF} \;-\; \delta_{\text{A}}\,A.$$

Here, the proliferation term $\rho_{\text{A}}\,A\cdot\text{CF}$ captures leukaemic expansion under space limitation, directly competing with normal haematopoietic cells, while $\delta_{\text{A}}A$ reflects natural death or clearance of AML cells[72,73,75,110].

5. Erythroblastic islands. Erythroblastic islands (EBIs) are specialised microenvironmental niches essential for efficient erythropoiesis[10,20]. The EBI population is governed by

$$\begin{aligned}\frac{d\text{EBI}}{dt} &= \rho_{\text{EBI}}\,\text{Nurse}\,(\text{ProE}+\text{BasoE}+\text{PolyE}+\text{OrthoE})\\ &\quad\times\left(1-\frac{\text{EBI}}{K_{\text{EBI}}\cdot\text{Nurse}}\right)-\delta_{\text{EBI}}\,\text{EBI}.\end{aligned}$$

Formation is modelled as depending on the interaction between Nurse cells and the total pool of developing erythroblasts, captured by the term $\rho_{\text{EBI}}\cdot\text{Nurse}\cdot(\text{ProE}+\text{BasoE}+\text{PolyE}+\text{OrthoE})$, and follows logistic growth limited by a carrying capacity proportional to the number of available Nurse cells, $\left(1-\frac{\text{EBI}}{K_{\text{EBI}}\cdot\text{Nurse}}\right)$. EBIs dissociate at rate $\delta_{\text{EBI}}\cdot\text{EBI}$.

6. Nurse macrophages. Nurse cells (specialised macrophages forming the EBI core) are regulated by:

$$\frac{d\text{Nurse}}{dt} \;=\; \rho_{\text{Nurse}}\,\text{Nurse}\cdot\text{CF} \;-\; \frac{\delta_{\text{Nurse}}\,\text{Nurse}}{1+\beta_{\text{Nurse}}^{\text{MCSF}}\,\text{MCSF}}.$$

The term $\rho_{\text{Nurse}}\cdot\text{Nurse}\cdot\text{CF}$ represents nurse influx/proliferation into the bone-marrow niche under the global space constraint (CF), while the death term indicates that Nurse survival is enhanced by macrophage colonystimulating factor (M-CSF), consistent with M-CSFs known supportive role for macrophages[46].

7. M-CSF dynamics. The dynamics of macrophage colony-stimulating factor (M-CSF), a cytokine critical for nurse cell survival and EBI stability, are described by:[20,46]

$$\frac{d\text{MCSF}}{dt} \;=\; \rho_{\text{MCSF}} \;-\; \delta_{\text{MCSF}}\,\text{MCSF} \;-\; \delta_{\text{MCSF,A}}\,\text{MCSF}\,\frac{A}{K}.$$

Here, ρ_{MCSF} is the constant baseline production rate and $\delta_{\text{MCSF}}\cdot\text{MCSF}$ is the natural degradation rate. The final term, $\delta_{\text{MCSF,A}}\cdot\text{MCSF}\cdot(A/K)$, accounts for AML-mediated removal of M-CSF. This reflects the mechanism by which leukaemic cells disrupt the bone marrow microenvironment, specifically targeting the M-CSF/Nurse axis, thereby destabilising EBIs and indirectly impairing erythropoiesis[9,108,111].

8. M-CSF therapeutic injection term. To simulate therapeutic administration of recombinant M-CSF, the baseline production rate is modified to be time-dependent:

$$\rho_{\mathrm{MCSF}}(t) \;=\; \rho_{\mathrm{MCSF}}^{\mathrm{base}} \;+\; \sum_i A_{\mathrm{MCSF}} \, \exp\!\left(-\frac{(t-t_i)^2}{w^2}\right) \, \mathbf{1}_{[t_i-\tau/2,\, t_i+\tau/2]}(t).$$

Here, $\rho_{\mathrm{MCSF}}^{\mathrm{base}}$ represents the endogenous baseline production. The summation term models the effect of repeated injections: A_{MCSF} is the amplitude or strength of each injection pulse, t_i is the centre time point of the i-th injection, w controls the width or sharpness of the Gaussian-like injection profile (governing rapid onset and decay), and τ defines the time window in which the injection is active. The indicator function $\mathbf{1}_{[t_i-\tau/2,\, t_i+\tau/2]}(t)$ restricts the injection effect to this specified interval, being equal to 1 if t falls within the dosing window and 0 otherwise.

This formulation captures the transient rise and fall in M-CSF concentration following injection, allowing simulation of therapeutic protocols involving single or repeated administrations.

3.2.2.3 Model Assumptions and Rationale

The model adopts simplifying but biologically motivated assumptions to capture key drivers of erythropoiesis and its disruption in AML while keeping the framework identifiable and computationally tractable.

Proliferation under niche limitation. Erythroid and leukaemic expansion are represented using first-order proliferation terms (ρX) constrained by a shared bone marrow capacity K through the competition factor (CF). This effective "logistic" limitation represents restricted space and support resources within the marrow and is consistent with prior haematopoietic and leukaemia modelling frameworks[74,77]. More flexible growth laws (e.g., Gompertz) were not used because the available data did not justify additional parameters.

Competition and carrying capacity. All proliferating populations compete within a normalised carrying capacity ($K = 1$), and CF scales proliferation according to total marrow occupancy. This aggregates spatial and cytokine-mediated competition into a single effective constraint, consistent with evidence that AML progressively saturates and remodels the niche[63,108,112]. Explicit spatial or multi-compartment niche structure could refine this interaction but was beyond the scope of the present study.

Spleen contribution. Extramedullary erythropoiesis is represented by a spleen source term that increases when bone marrow output is compromised, capturing compensatory dynamics during stress[10,36,101]. Because quantitative data for AML-specific splenic output are limited, this component should be interpreted as a phenomenological approximation rather than a directly calibrated estimate.

Cytokine feedback and macrophage interactions. Cytokine regulation (e.g., M-CSF and representative inflammatory mediators such as IL-6) is encoded using linear or saturating relationships reflecting reported stimulatory and inhibitory interactions in macrophage–erythroid biology[113–115]. More detailed nonlinear kinetics (e.g., Hill functions) were not implemented owing to limited dose–response constraints but could be incorporated in future work.

Scope of the framework. The model does not explicitly represent systemic erythropoietin control, iron hormones, or stromal heterogeneity. Instead, these influences are absorbed into aggregate feedback parameters, with the primary aim of quantifying how AML-driven niche remodelling alters erythroid output.

3.2.3 Definition and Biological Interpretation of Parameters

This section summarises the biological meaning of all parameters in the mathematical model of bone marrow erythropoiesis under leukaemic and non-leukaemic conditions. Each parameter represents a specific process (e.g., proliferation, differentiation, attrition, or niche-mediated regulation) and is linked to a defined cellular compartment or regulatory factor. Parameter ranges and baseline values were informed by the available experimental datasets (flow cytometry, RNA-seq, and M-CSF treatment assays) and by established modelling studies of haematopoiesis and AML[69,76,116]. For clarity, parameters are grouped below by functional role.

Proliferation rates (ρ)

Proliferation parameters define the intrinsic expansion capacity of each compartment. At the top of the hierarchy, ρ_{LKS}, ρ_{CMP}, and ρ_{MEP} control growth of stem and progenitor pools, reflecting the balance between self-renewal and progenitor amplification. Within the erythroid lineage, ρ_{ProE}, ρ_{BasoE}, and ρ_{PolyE} govern erythroblast expansion, with effective proliferation modulated by erythroblastic island (EBI) support in the model. Niche dynamics are captured by ρ_{EBI}, representing EBI formation through macrophage–erythroblast interactions, and by ρ_{Nurse}, describing baseline maintenance of nurse macrophages under space and survival constraints. AML blast expansion is governed by ρ_{A}, tuned to reproduce aggressive leukaemic growth. Cytokine production is represented by ρ_{MCSF}, the baseline M-CSF production rate. Finally, ρ_{spleen} represents the compensatory splenic contribution to RBC production, which increases during AML-associated anaemia.

Differentiation rates (γ)

Differentiation parameters govern lineage progression between compartments. Commitment towards erythropoiesis is described by $\gamma_{\mathrm{LKS}\to\mathrm{CMP}}$, $\gamma_{\mathrm{CMP}\to\mathrm{MEP}}$, and $\gamma_{\mathrm{MEP}\to\mathrm{ProE}}$. Sequential erythroblast maturation is captured by $\gamma_{\mathrm{ProE}\to\mathrm{BasoE}}$, $\gamma_{\mathrm{BasoE}\to\mathrm{PolyE}}$, and $\gamma_{\mathrm{PolyE}\to\mathrm{OrthoE}}$, while terminal maturation into circulating red blood cells is governed by $\gamma_{\mathrm{OrthoE}\to\mathrm{R}}$. In erythroid compartments, differentiation is modulated by β^{γ}, representing nurse macrophage/EBI-driven enhancement of maturation[20,95,97].

Death rates (δ)

Attrition parameters represent loss through apoptosis, clearance, or functional exhaustion. Stage-specific turnover is encoded by δ_{LKS}, δ_{CMP}, δ_{MEP}, δ_{ProE}, δ_{BasoE}, δ_{PolyE}, δ_{OrthoE}, and δ_{R}. Niche turnover is captured by δ_{EBI} (EBI disassembly) and δ_{Nurse} (nurse macrophage attrition), with nurse survival partially protected by M-CSF in the model. Leukaemic blast turnover is governed by δ_{A}. M-CSF kinetics include basal degradation (δ_{MCSF}) and an AML-associated component ($\delta_{\mathrm{MCSF,A}}$) that represents leukaemia-driven reduction in M-CSF availability under increasing leukaemic burden[108].

Regulatory coefficients and interaction terms

Niche-dependent regulation is encoded through interaction coefficients that modify erythroid kinetics. The parameters β^{ρ} and β^{γ} scale the extent to which erythroblastic islands (EBIs) enhance erythroblast proliferation and differentiation, respectively, thereby representing microenvironmental amplification of erythropoiesis. The protective effect of M-CSF on nurse macrophages is captured by $\beta_{\mathrm{MCSF,Nurse}}$, which determines how strongly M-CSF reduces effective nurse macrophage attrition. In addition, K_{EBI} defines the saturation capacity of EBIs relative to nurse macrophage availability, limiting EBI formation under niche saturation.

Capacity constraints

The bone marrow is modelled as a shared, space-limited environment with total carrying capacity K (normalised to 1). Competition for this shared space is implemented via the competition factor CF, which reduces proliferation in proportion to total marrow occupancy and couples the growth of all proliferating compartments.

Injection-related parameters

Therapeutic M-CSF simulations introduce parameters for exogenous administration. The pulse amplitude is set by A_{MCSF}, injections are applied at discrete time points t_i, and each pulse is characterised by a duration τ. A Gaussian width parameter w is used to approximate smooth injection profiles for numerical stability.

3.2.4 Model Parameter Ranges Justification

Model parameters were optimised within biologically plausible ranges informed by experimental and theoretical studies of haematopoiesis. Where available, bounds were anchored to published estimates, such as red blood cell lifespan[117] and proliferation rates for erythroid progenitors[118,119]. Where direct estimates were unavailable, broader ranges were assigned to reflect uncertainty and biological variability. Parameter definitions and justifications are documented in Table 3.1 and its cited sources[74,75,117,118].

All priors were defined in $\log_{10}$ space to ensure positivity and to accommodate order-of-magnitude uncertainty across kinetic processes.

Notation and grouping. Proliferation rates are denoted by ρ (e.g., ρ_{LKS}), decay/death rates by δ (e.g., δ_{MEP}), and differentiation rates by γ (e.g., $\gamma_{\mathrm{LKS}\to\mathrm{CMP}}$). Regulatory coefficients β quantify niche-mediated modulation of erythroblast proliferation and differentiation via EBIs (e.g., $\beta^{\rho}_{\mathrm{ProE}}$ and $\beta^{\gamma}_{\mathrm{BasoE}}$), representing nurse macrophage/EBI support.

Extrinsic regulation by M-CSF is represented through ρ_{MCSF}, δ_{MCSF}, $\delta_{\mathrm{MCSF\_A}}$, and $\beta_{\mathrm{MCSF,Nurse}}$, capturing baseline cytokine dynamics and AML-mediated depletion. In therapeutic simulations, $\rho_{\mathrm{MCSF}}(t)$ is augmented by exogenous pulses to reflect the injection schedule.

Mapping of log-space priors. All bounds are reported as ($\log_{10}$ min, $\log_{10}$ max), with natural units obtained via $x \in [10^{\log_{10}\min}, 10^{\log_{10}\max}]$[68,69,74,75].

Table 3.1: Parameter ranges used in the model ($\log_{10}$ scale), units, and source justification.

Parameter	Log_{10} Range	Units	References / Justification
ρ_{LKS}	(-3.7, -2.3)	h^{-1}	50,120,121
ρ_{spleen}	(-5.0, -0.5)	h^{-1}	Stress erythropoiesis scaling;[36,39]
ρ_{CMP}	(-2.0, -1.1)	h^{-1}	122,123
ρ_{MEP}	(-2.0, -1.2)	h^{-1}	122,123
ρ_{ProE}	(-1.0, -0.8)	h^{-1}	123,124
ρ_{BasoE}	(-1.0, -0.8)	h^{-1}	10,125,126
ρ_{PolyE}	(-1.3, -1.0)	h^{-1}	10,126
ρ_{OrthoE}	(-10, -3)	h^{-1}	Very low proliferation;[10,124,127]
ρ_{EBI}	(-10, -1.6)	h^{-1}	Island formation kinetics;[10,101]
ρ_{Nurse}	(-3.0, -1.5)	h^{-1}	101
δ_{LKS}	(-4.0, -2.0)	h^{-1}	128–133
δ_{CMP}	(-4.0, -2.0)	h^{-1}	130,133,134
δ_{MEP}	(-5.0, -3.0)	h^{-1}	134,135
δ_{ProE}	(-4.0, -1.0)	h^{-1}	119,133
δ_{BasoE}	(-5.0, -2.0)	h^{-1}	119,135
δ_{PolyE}	(-5.0, -3.0)	h^{-1}	119,136
δ_{OrthoE}	(-6.0, -4.0)	h^{-1}	119,137
δ_{EBI}	(-5.0, -3.0)	h^{-1}	Island turnover;[119,131,137]
δ_{Nurse}	(-5.0, -3.0)	h^{-1}	M-CSFsensitive attrition;[119,131,137]
δ_{A}	(-3.0, -2.0)	h^{-1}	AML turnover;[6]
δ_{R}	(-3.5, -2.5)	h^{-1}	RBC lifespan scaling;[117,138]
K_{EBI}	(-7.3, -6.5)	dimensionless	Estimated from island counts vs. nurse supply
ρ_{A}	(-2.0, -1.0)	h^{-1}	AML growth;[72,73,75]
$\beta_{\text{ProE\_}\rho}$	(-5.0, 5.0)	dimensionless	EBI modulation, uninformative prior
$\beta_{\text{ProE\_}\gamma}$	(-5.0, 5.0)	dimensionless	EBI modulation, uninformative prior
$\beta_{\text{BasoE\_}\rho}$	(-5.0, 5.0)	dimensionless	EBI modulation, uninformative prior
$\beta_{\text{BasoE\_}\gamma}$	(-5.0, 5.0)	dimensionless	EBI modulation, uninformative prior
$\beta_{\text{PolyE\_}\rho}$	(-5.0, 5.0)	dimensionless	EBI modulation, uninformative prior
$\beta_{\text{PolyE\_}\gamma}$	(-5.0, 5.0)	dimensionless	EBI modulation, uninformative prior
$\beta_{\text{OrthoE\_}\rho}$	(-5.0, 5.0)	dimensionless	EBI modulation, uninformative prior
$\beta_{\text{OrthoE\_}\gamma}$	(-5.0, 5.0)	dimensionless	EBI modulation, uninformative prior
$\gamma_{\text{LKS}\to\text{CMP}}$	(-3.1, -2.2)	h^{-1}	49,139,140
$\gamma_{\text{CMP}\to\text{MEP}}$	(-2.3, -1.3)	h^{-1}	141
$\gamma_{\text{MEP}\to\text{ProE}}$	(-1.9, -1.3)	h^{-1}	69,118,123
$\gamma_{\text{ProE}\to\text{BasoE}}$	(-1.2, -0.8)	h^{-1}	69,118,142
$\gamma_{\text{BasoE}\to\text{PolyE}}$	(-1.2, -0.8)	h^{-1}	69,118,142
$\gamma_{\text{PolyE}\to\text{OrthoE}}$	(-1.2, -0.7)	h^{-1}	69
$\gamma_{\text{OrthoE}\to\text{R}}$	(-1.3, -0.7)	h^{-1}	69,118
ρ_{MCSF}	(6.0, 9.0)	h^{-1}	Production scaling;[143–145]
δ_{MCSF}	(-1.0, 0.6)	h^{-1}	Clearance;[146–149]
$\beta_{\text{MCSF\_Nurse}}$	(-12.0, -6.0)	molecule^{-1}	Survival sensitivity, uninformative prior
$\delta_{\text{MCSF\_A}}$	(-4.0, -1.0)	$\text{cell}^{-1}{\cdot}h^{-1}$	AML-associated consumption;[143]

These priors support robust parameter estimation (model fitting) and global sensitivity analyses (VARS, PCESobol, eFAST) described in Sections 2.42.6, ensuring fair cross-method comparison under consistent computational budgets. Each parameter in the model corresponds to a biologically meaningful process, from stem cell proliferation to erythroblast differentiation, niche interaction, and cytokine regulation. The structure of the model allows investigation into how AML-induced changes-such as loss of EBIs or disruption of macrophage-supportive cytokine signalling (modelled here via altered M-CSF availability)-drive the collapse of erythropoiesis. When calibrated against experimental data, these parameters enable simulations that predict therapeutic outcomes and identify sensitive targets in the system.

3.2.5 Simulation Framework and Computational Tools

Simulation, calibration, and sensitivity analyses were implemented in *Julia*. The ODE system was solved using `DifferentialEquations.jl`[150], employing the stiff solver TRBDF2 (trapezoidal rule + second-order backward differentiation formula) for stable integration of

tightly coupled dynamics[150]. Simulations were run over a 32-day period, initialised under baseline (non-AML) conditions, with AML introduced at varying levels. Model outputs were summarised as fold changes relative to controls to quantify AML-induced disruption of erythropoiesis.

Parameter optimisation was performed with the Exponential Natural Evolution Strategy (xNES)[151,152], implemented in Julia[152]. xNES adapts a multivariate Gaussian search distribution over the parameter space, enabling derivative-free optimisation in high dimensions. The objective function was a weighted mean squared error (WMSE) between simulated and experimental fold-change profiles, with weights correcting for imbalances in measurement availability across AML conditions.

The Julia workflow integrated simulation (`DifferentialEquations.jl`), optimisation (`BlackBoxOptim.jl`)[151,153], and visualisation (`Plots.jl`, `StatsPlots.jl`). Reproducibility was supported by fixed random seeds, saving intermediate parameter sets, and containerised environments. Surrogate modelling for global sensitivity analysis (e.g., Polynomial Chaos Expansion) was prepared using `Surrogates.jl`, with parallel execution to reduce runtime[154].

3.2.6 Initial Conditions

Initial conditions were chosen to reflect the hierarchical structure of haematopoiesis while respecting the bone marrow (BM) capacity constraint. With the carrying capacity normalised to $K = 1$, all compartments were initialised as fractions of total BM capacity (Table 3.2)[72,106]. The initial values follow the expected ordering (rare stem/progenitor cells, progressively larger erythroblast pools, and abundant circulating red blood cells), providing a biologically plausible baseline for calibration and simulation. Because variables are normalised to K, these fractions are heuristic rather than direct cell-count measurements and were selected to keep total occupancy below capacity, leaving space for AML seeding and niche dynamics.

The AML initial condition $A(0)$ was varied across simulations to investigate the impact of leukaemic burden on erythropoiesis and on the predicted efficacy of M-CSF therapy. M-CSF was initialised at its no-AML steady state, $\mathrm{MCSF}(0) = \rho_{\mathrm{MCSF}}/\delta_{\mathrm{MCSF}}$, representing physiological baseline signalling prior to disease onset.

Control (no-AML) steady states were not used as initial conditions when introducing AML. Because proliferation is scaled by the global competition factor (CF), seeding AML onto a near-capacity steady state can push total occupancy towards or beyond K, causing abrupt and non-physiological suppression of proliferation (and potential numerical stiffness near capacity). Instead, biologically motivated initial fractions were used to preserve realistic proportions while maintaining headroom for AML expansion[74,76].

Table 3.2: Initial conditions for model variables with biological rationale. Values are normalised initial conditions; haematopoietic and niche populations are expressed as fractions of the BM capacity $K = 1$, while R represents a normalised output compartment for circulating RBCs.

Value	Cell Population	Biological Rationale	Reference
0.01	LKS (stem cells)	HSCs are rare in adult BM; initialised as a small fraction of total capacity.	49,140
0.02	CMP	Myeloid progenitors are more frequent than HSCs due to early amplification.	140,155
0.03	MEP	Erythroid commitment proceeds via MEP expansion downstream of CMP.	155,156
0.05	ProE	First committed erythroid precursor stage; expansion begins in early erythroid compartments.	123,125
0.08	BasoE	Early erythroblasts are proliferative and expand relative to ProE.	119,123
0.12	PolyE	Intermediate erythroblasts continue expansion before terminal maturation.	119,123
0.15	OrthoE	Late erythroblasts approach terminal differentiation and enucleation.	10,119
0.40	R (RBCs)	Large terminal/output compartment in the normalised model representing dominant erythroid output.	30
$0.1 \cdot K_{\mathrm{EBI}}$	EBI	Islands start below saturation (here $\sim 10\%$) to allow niche formation dynamics.	10,101
0.03	Nurse cells	Nurse macrophages are a minority niche-supporting population; initialised at a small fraction.	10,20,101
$\rho_{\mathrm{MCSF}}/\delta_{\mathrm{MCSF}}$	M-CSF	Initialised at steady state (baseline production over degradation) before AML perturbation.	98,144

3.3 Model Simulations and Calibration

The ODE model was implemented in *Julia* using `DifferentialEquations.jl` and integrated with the stiff solver TRBDF2, which is well suited to nonlinear systems with coupled feedback and disparate time scales[150]. A control simulation without AML ($A(0) = 0$) defined baseline output levels. Disease simulations were then run for 32 days across a range of initial AML burdens $A(0)$, matching the 3–4 week monitoring window of the MLL-AF9 *in vivo* experiments. For each burden, terminal population sizes were converted to fold changes relative to control.

Parameter estimation was performed using the Exponential Natural Evolution Strategy (xNES)[152]. Model fit was evaluated using a weighted mean squared error (WMSE) between simulated and experimental fold changes, with weights correcting for unequal sample counts across AML infiltration groups. Search bounds were defined by the biologically plausible priors in Table 3.1. The resulting calibrated parameter sets were used for model validation and subsequent sensitivity analyses.

3.3.1 Validation Metrics and Robustness of the Model

Model validation compared simulated outputs with experimental measurements from AML mouse models, including erythroid populations (ProE, BasoE, PolyE, OrthoE), nurse macrophages/EBIs, and total RBC output, quantified by flow cytometry, imaging flow cytometry, and transcriptomic profiling. Model agreement was assessed using the weighted mean squared error (WMSE), defined as the mean squared deviation between simulated and experimental fold changes across measured cell types, with weights correcting for unequal sampling across AML infiltration groups[157,158]. This weighting prevents error estimates from being dominated by data-rich conditions[157].

Robustness was evaluated by running simulations over multiple parameter sets drawn from the prior ranges (Table 3.1) and retaining only solutions achieving low WMSE after optimisation with the Exponential Natural Evolution Strategy (xNES)[159]. Local perturbations of best-fitting parameter sets were then used to confirm that key qualitative behaviours (early erythroid collapse at low AML burden, nonlinear suppression of late erythroblast stages, and partial rescue following M-CSF supplementation) were preserved under small parameter changes.

To assess generalisation, predictions were additionally evaluated at AML infiltration levels not used during calibration[159]. Together, WMSE-based fitting, perturbation testing, and out-of-sample evaluation support the use of the calibrated model for exploratory simulation and sensitivity analyses.

3.3.1.1 Local Sensitivity Analysis (LSA)

Local sensitivity analysis (LSA) was used to quantify the effect of small, one-at-a-time parameter perturbations around the calibrated best-fitting parameter set. Each parameter θ_i was perturbed by a small relative amount (typically $\pm 1\%$) while all other parameters were held fixed. Sensitivity was computed using the normalised finite-difference index:

$$S_i^{\text{local}} = \frac{\Delta Y / Y}{\Delta \theta_i / \theta_i},$$

where Y denotes an output of interest (e.g., erythroid compartments, RBCs, Nurse/EBI abundance, or AML burden). Outputs were evaluated at $t = 32$ days to match the endpoint fold-change summaries used for calibration[159].

Parameters with large $|S_i^{\text{local}}|$ were interpreted as strong local drivers at the calibrated operating point, indicating whether proliferation, differentiation, niche support (M-CSF/Nurse/EBI), or leukaemic competition dominated the response. As LSA does not capture interactions or nonlinear effects away from the reference point, it was used as an initial diagnostic prior to global sensitivity analyses (VARS, PCE–Sobol, and eFAST).

We additionally verified that $\pm 1\%$ perturbations did not induce numerical instability and that sensitivity signs were consistent for positive and negative perturbations.

3.3.1.2 One-At-a-Time (OAT) Sensitivity Analysis

One-at-a-Time (OAT) sensitivity analysis was used to quantify the effect of finite, single-parameter changes on model behaviour, holding all other parameters at their calibrated values. Unlike local sensitivity analysis, which probes infinitesimal perturbations, OAT sweeps can reveal non-monotonic responses and threshold-like behaviour under larger deviations[160,161].

For each parameter θ_i, three sweep regimes were performed: (i) $\pm 10\%$, (ii) $\pm 50\%$, and (iii) the full prior range (Table 3.1). For each sweep value, the model was re-simulated over 32 days and evaluated using the objective function J (Section 2.2.5). To prevent extreme objective values from dominating rankings, J was transformed using a fixed sigmoid function to obtain $\tilde{J}$. Sensitivity curves were plotted against the log-scaled parameter value, and an OAT score was computed as:

$$S_i^{\text{OAT}} = \text{Var}\Big(\tilde{J}(\theta_i)\Big).$$

OAT results provide single-parameter influence rankings and were used as a diagnostic step prior to global methods (VARS, PCE–Sobol, and eFAST). As OAT does not capture parameter interactions, it can underestimate effects driven primarily by synergistic or higher-order pathways[160,162].

3.3.2 Comparison with Experimental AML Data

Model outputs were compared with *in vivo* measurements from the MLL-AF9 AML mouse model to assess whether simulations reproduced key biological trends across increasing leukaemic burden[20]. Experimental readouts included haematopoietic stem and progenitor compartments (LKS, CMP, MEP), erythroid maturation stages (ProE, BasoE, PolyE, OrthoE), and niche-associated components (EBIs and nurse macrophages), quantified by flow cytometry and imaging flow cytometry[20]. Samples spanned early disease (approximately 2–15% marrow infiltration) through advanced disease exceeding 80–90%[20]. Transcriptomic profiling of sorted nurse macrophages provided complementary evidence for niche alterations under leukaemic stress[20].

To mirror these conditions *in silico*, simulations were initialised with AML burdens corresponding to the experimentally defined infiltration groups. For each condition, fold changes were computed relative to a non-leukaemic baseline and compared directly with experimental fold-change measurements.

Across the burden range, simulations reproduced hallmark features of AML-associated marrow dysfunction, including early loss of erythroid populations (from ProE onwards) even at relatively low AML infiltration[20]. Upstream compartments (LKS, CMP, MEP) showed a more gradual decline with increasing burden. The model also predicted collapse of EBIs and attrition of nurse macrophages, coinciding with a non-linear reduction in RBC output, supporting the interpretation that erythropoietic failure is driven primarily by niche disruption rather than space competition alone[20,108,111,163]. Mechanistically, these effects were represented through AML-driven depletion of M-CSF, linking leukaemic burden to nurse macrophage survival and EBI stability[20,46].

Quantitative agreement was summarised using the weighted mean squared error (WMSE), which accounts for unequal sample sizes across infiltration groups. For most compartments and conditions, simulated fold changes were consistent with the variability observed across biological replicates, supporting the use of the calibrated model for subsequent sensitivity analyses and predictive simulations.

3.4 Global Sensitivity Analysis: Concept and Classification

Global Sensitivity Analysis (GSA) was used to attribute uncertainty in model outputs to uncertainty in model parameters across their biologically plausible ranges. Unlike local or one-at-a-time analyses, GSA explores the full parameter space and therefore captures nonlinear responses and interaction effects[162,164]. Its core principle is variance decomposition, in which the variance of a model output is partitioned into contributions from individual parameters and from their interactions, enabling parameters to be ranked by influence[162,164].

In this study, four complementary GSA approaches were implemented. Sobol indices were used as the benchmark variance-based method, providing first-order and total-order measures of parameter importance[162,164]. As a computationally cheaper variance-based alternative, the Extended Fourier Amplitude Sensitivity Test (eFAST) was employed using spectral (frequency-domain) variance decomposition[162,165]. A surrogate-based Polynomial Chaos Expansion (PCE) was applied to approximate the response surface and estimate first-, second-, and total-order Sobol indices efficiently using a degree-2 expansion[166]. Finally, Variogram Analysis of Response Surfaces (VARS) was implemented as a variogram-based framework for efficient total-order screening in high-dimensional settings under constrained computational budgets[167].

Summary. Using these methods side by side provided a robust ranking of parameter influence and enabled fair comparison under matched computational budgets.

3.4.1 Local vs. Global Sensitivity Analysis

Local Sensitivity Analysis (LSA) evaluates parameter influence around a single reference point (here, the calibrated best-fitting parameter set). It quantifies how small perturbations in a parameter θ_i change a model output y, typically using derivatives or finite differences, for example:

$$\frac{\partial y}{\partial x_i} \approx \frac{f\left(x_1, \ldots, x_i + \Delta x, \ldots, x_n\right) - f\left(x_1, \ldots, x_i, \ldots, x_n\right)}{\Delta x}.$$

LSA is computationally inexpensive and provides point-specific insight, but it does not capture nonlinearities or parameter interactions away from the reference point[162,168,169].

Global Sensitivity Analysis (GSA), in contrast, quantifies parameter influence across the full input distribution, explicitly accounting for nonlinear responses and higher-order interactions. This is essential for the erythropoiesis model, where feedback mechanisms (e.g., EBI modulation, AML competition, and M-CSF signalling) generate non-additive behaviour that local perturbations may miss[162,164].

In this study, LSA and one-at-a-time (OAT) analyses were used as preliminary diagnostics, while GSA formed the primary analytical framework. Variance-based Sobol indices, spectral eFAST, polynomial chaos expansion (PCE; degree 2), and variogram-based VARS were implemented to provide complementary perspectives on parameter importance under matched computational budgets[164–167].

3.4.2 Variance-Based Global Sensitivity Analysis (Sobol, eFAST, PCE, VARS, IVARS)

Variance-based Global Sensitivity Analysis (GSA) attributes uncertainty in a model output $Y = f(X)$ to uncertainty in the inputs by analysing the output variance $V(Y)$. This provides a global ranking of parameters based on main effects and interaction effects[164].

Sobol indices. Classical Sobol analysis was used as the reference variance-decomposition approach. The first-order index S_i quantifies the main effect of X_i on Y:

$$S_i = \frac{V(\mathbb{E}[Y \mid X_i])}{V(Y)}.$$

Total-order effects were also considered to capture the contribution of X_i including interactions[164].

eFAST. As a computationally efficient alternative, the Extended Fourier Amplitude Sensitivity Test (eFAST) was employed. eFAST assigns each input a distinct sinusoidal frequency and estimates sensitivity by decomposing the output variance in the frequency domain, providing efficient estimation of (first- and) total-order effects while remaining sensitive to nonlinear and interaction-driven behaviour[162,165,169].

Polynomial Chaos Expansion (PCE). To reduce computational cost further, a surrogate-based Polynomial Chaos Expansion (PCE) was adopted. The model response is approximated using orthogonal polynomial basis functions:

$$Y = \sum_{\alpha} c_\alpha \Psi_\alpha(X).$$

Sobol indices can then be computed analytically from the expansion coefficients. A degree-2 PCE was constructed to estimate first-order, second-order, and total-order indices[166,170].

VARS and IVARS. Variogram Analysis of Response Surfaces (VARS) was implemented as an alternative global framework that quantifies sensitivity via the spatial variability of the response surface. For an input parameter X_i, the directional variogram is defined as:

$$\gamma(h_i) = \frac{1}{2}\,\mathbb{E}\Big[\big(Y(X + h_i\mathbf{e}_i) - Y(X)\big)^2\Big].$$

VARS employs star-based sampling designs to estimate total-order effects efficiently, making it well suited to high-dimensional models under constrained computational budgets[167]. Integrated VARS (IVARS) was also computed to summarise sensitivity across multiple perturbation scales by integrating the variogram over a range of step sizes (e.g., IVARS_{10}, IVARS_{30}, IVARS_{50})[167].

Implementation. To support these analyses, we developed a Julia package, `VariogramAnalysis.jl`, to implement VARS and its extensions, including star-based sampling, variogram/eco-variogram computation, and bootstrap-based uncertainty estimation and ranking. The implementation is independent of the Python `varstool`[171] and was validated by comparison with Python results on benchmark models (e.g., Ishigami and Sobol–G), confirming numerical consistency[164,172,173].

Overall, Sobol indices provided the benchmark variance decomposition, eFAST offered an efficient spectral alternative, PCE enabled surrogate-based variance decomposition, and VARS/IVARS provided robust high-dimensional screening under limited computational budgets.

3.4.3 Choosing the Right GSA Method

The choice of global sensitivity analysis (GSA) method in this study was driven by the dimensionality of the parameter space, the computational budget, and the type of sensitivity information required. Methods were benchmarked under matched computational cost, comparing Sobol indices, eFAST, polynomial chaos expansion (PCE), and the variogram-based VARS approach.

Sobol indices provide the reference standard, yielding first-order (S_1), second-order (S_2), and total-order (S_T) effects[164]. However, they scale poorly with increasing dimensionality because common estimators require $(d+2)N$ model evaluations[162,174].

The eFAST method estimates S_T (and, in part, S_1) using $N \times d$ samples, making it practical for low- to medium-dimensional problems but increasingly costly as d grows[162,165,169].

PCE (degree 2) offers a full variance decomposition (S_1, S_2, S_T) with moderate computational demand[166]. Because the indices are extracted analytically from the surrogate coefficients, PCE provides an efficient option when a more complete sensitivity profile is needed for nonlinear models.

By contrast, VARS targets total-order effects and can be substantially more sample-efficient due to star-based sampling and variogram analysis[167,175]. This makes VARS well suited to high-dimensional screening under constrained budgets. Integrated variants such as IVARS summarise variogram information across perturbation scales[167].

In summary, no single GSA method is universally optimal. Sobol remains the gold standard for comprehensive variance decomposition[164]; PCE provides an efficient middle ground with full sensitivity profiles[166]; eFAST is best suited to lower dimensions[162,165]; and VARS offers a computationally efficient alternative for high-dimensional screening[167]. A comparative summary of these methods, including sensitivity indices, computational cost, and efficiency, is presented in Section 3.6.2 (Table 4.1).

3.5 Sampling Techniques for Global Sensitivity Analysis

Efficient sampling is essential for estimating sensitivity indices within a limited computational budget. In this study, three sampling approaches were used: Sobol-type variance-based sampling, eFAST frequency-based sampling, and the star-based sampling strategy used by VARS. Polynomial Chaos Expansion (PCE) differs from these designs because it constructs a surrogate response surface and derives sensitivity indices from the expansion coefficients[166].

3.5.1 Sobol Sampling Designs

Variance-based Sobol analysis uses structured sampling designs to estimate first-order and total-order indices via Monte Carlo estimators[164]. Here, low-discrepancy (quasi-random) sampling was used to improve coverage of the parameter space and stabilise index estimates compared with purely random draws.

3.5.2 eFAST Sampling

The Extended Fourier Amplitude Sensitivity Test (eFAST) applies periodic sampling, assigning each input parameter a distinct frequency. Model outputs are analysed in the frequency domain to attribute variance to individual parameters and their interactions, enabling efficient estimation of sensitivity indices at moderate computational cost[162,165].

3.5.3 VARS Sampling Strategy

VARS uses a star-based design in which star centres are generated in the parameter space and one-dimensional trajectories are constructed along each parameter direction. Evaluations along these rays are used to compute variograms, from which total-order sensitivity measures can be estimated efficiently, making VARS well suited to high-dimensional screening under limited budgets[167].

3.5.4 Note on PCE

Polynomial Chaos Expansion (PCE) represents the model output as an expansion in orthogonal polynomials of the inputs, allowing Sobol-type sensitivity indices to be computed analytically from the expansion coefficients[166]. In this study, a degree-2 PCE was used to obtain first-, second-, and total-order indices with reduced model-evaluation cost compared with direct variance-based estimators.

3.6 Benchmark (Toy) Models for Method Testing

Benchmark (toy) models were used to validate and compare global sensitivity analysis (GSA) methods under controlled conditions. These test functions and simple dynamical systems provide standardised settings for assessing numerical accuracy, convergence behaviour, and computational efficiency before applying the methods to the full erythropoiesis model.

3.6.1 Sobol G-function

The Sobol G-function is a standard benchmark in variance-based GSA. It maps independent inputs $x_i \sim U[0,1]$ to an output whose sensitivity structure is controlled by parameters $a_i \geq 0$, where larger a_i values reduce the influence of input x_i. Because the corresponding sensitivity indices can be obtained analytically, it is widely used to verify numerical implementations of variance-based methods[164].

In this project, the Sobol G-function was used to validate Sobol, eFAST, and PCE implementations (using analytical indices as reference) and to test the `VariogramAnalysis.jl` workflow. Cross-method comparisons under matched computational budgets were executed via distributed Julia scripts (e.g., `sobol_g_comparison_with_other_GSAs.jl`), with results reported in Section 3.4.

3.6.2 Exponential Decay Model

The exponential decay model is a simple ODE with two parameters:

$$\frac{dy(t)}{dt} = -k\, y(t), \qquad y(0) = y_0.$$

As a smooth, low-interaction dynamical system, it provides a sanity check that GSA methods behave sensibly on time-dependent outputs. Comparative experiments were run in Julia (`exponential_decay_different_dimensions.jl`) by varying the input dimensionality (e.g., $d = 3, 10, 20, 40$) and applying Sobol, eFAST, PCE (degree 2), and VARS under matched computational budgets. Results are reported in Section 3.4.2.

3.6.3 Morris Test Function

A Morris-type benchmark was used to evaluate screening behaviour under controlled main and interaction effects. The test function was constructed as a polynomial in transformed inputs $w_i \in [0, 1]$, with tunable coefficients controlling the strength of additive and higher-order interaction terms. This enables assessment of whether methods distinguish influential from non-influential parameters.

3.6.4 Implementation and Parallelisation

Benchmarking experiments were executed in Julia using `Distributed.jl` for parallel execution. Low-discrepancy designs were generated via `QuasiMonteCarlo.jl` for consistent sampling across methods. Distributed execution reduced runtime when repeating experiments across benchmark models and dimensions, supporting robust comparisons under matched computational budgets.

The `VariogramAnalysis.jl` package formalised these workflows by providing modules for sampling, variogram-based analysis, bootstrap uncertainty estimation, and regression tests on benchmark models prior to applying the methods to the erythropoiesis case study.

Results

4.1 Calibrated mathematical model simulations capture AML-induced disruption of erythropoiesis

The calibrated parameter set fit the experimental fold-change data, as quantified by the weighted mean squared error (WMSE) and illustrated by the model–data agreement in Figure 4.1. Simulations reproduced baseline erythropoiesis and its disruption by AML: increasing marrow infiltration led to progressive reductions across erythroid compartments, consistent with AML-associated marrow failure. The results support the hypothesis that erythroblastic island (EBI) dysfunction is a primary driver of erythropoietic failure in acute myeloid leukaemia[20].

Across compartments, the model captured the stage-specific pattern that late erythroid populations are more sensitive to AML burden than early progenitors. For example, reticulocytes (RETs) declined more steeply than megakaryocyte–erythroid progenitors (MEPs) as AML percentage increased (Figure 4.2), consistent with experimental observations[20].

The model also predicted a progressive collapse of EBIs with increasing AML burden, with the steepest decline between approximately 45–80% marrow infiltration (Figure 4.3). This supports a niche-centric interpretation in which erythropoietic suppression arises primarily from disrupted macrophage-supported erythroid maturation rather than blast crowding alone[20].

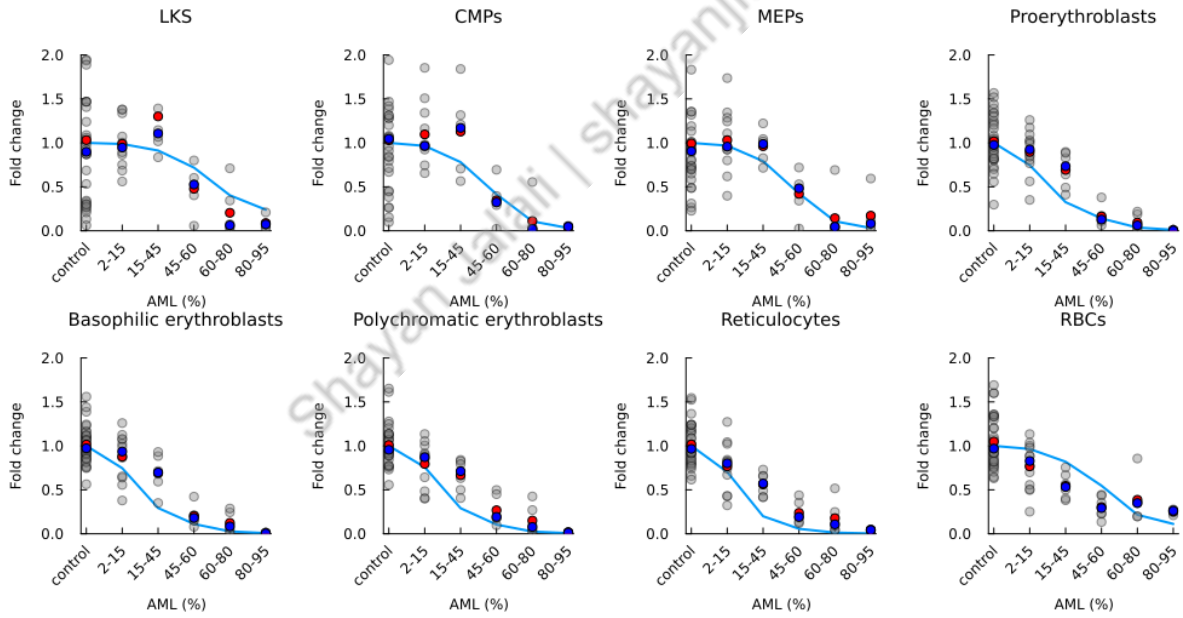

Figure 4.1: Fold changes in erythroid progenitor populations as a function of AML percentage. The model simulations (blue lines) closely match the experimental data (grey circles). Panels display results for LKS, CMPs, MEPs, ProE, BasoE, PolyE, OrthoE, RETs, and RBCs.

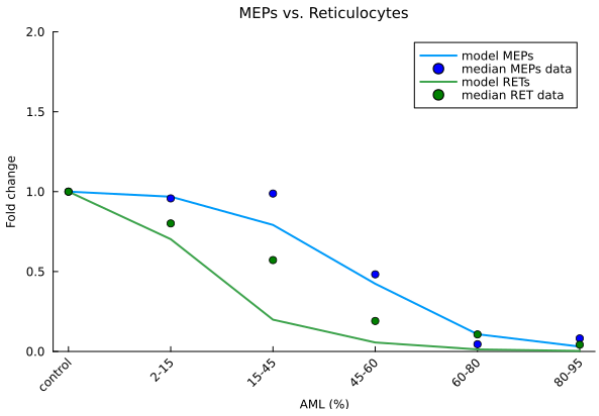

Figure 4.2: Model prediction and experimental validation that reticulocytes (RETs) are more sensitive to AML burden than megakaryocyte–erythroid progenitors (MEPs). RETs decline more steeply with increasing AML, reflecting selective vulnerability of late erythroid stages.

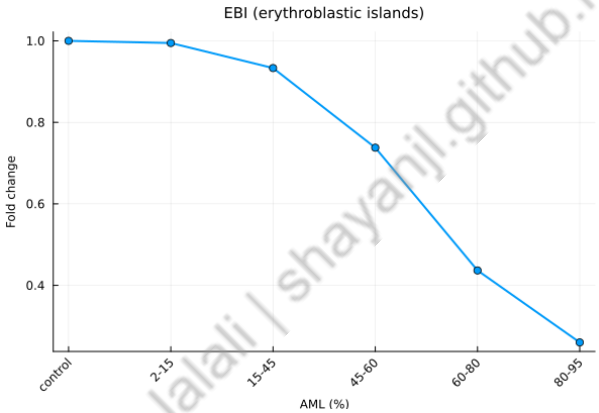

Figure 4.3: Calibrated model predicts AML drives loss of erythroblastic islands (EBIs). The sharpest decline occurs between AML infiltration levels of 45–80% of bone marrow, supporting niche collapse as a driver of erythropoietic suppression.

Taken together, the simulations suggest a coherent sequence of niche-mediated disruption in AML: leukaemic progression reduces macrophage-supportive signalling, leading to nurse macrophage loss, EBI destabilisation, and impaired terminal erythroid maturation. This provides a mechanistic explanation for the experimentally observed non-linear decline in late-stage erythroid output and supports niche-directed therapeutic strategies aimed at restoring macrophage support.

Overall, the results indicate that AML-associated erythropoietic failure is driven primarily by niche disruption rather than simple space competition, providing a mechanistic basis for the subsequent analysis of EBI-dependent regulation.

4.2 Modelling reveals EBIs preferentially promote differentiation over proliferation

Having validated the model against experimental data, we examined the fitted β parameters, which quantify EBI-mediated modulation of proliferation (ρ) and differentiation (γ) rates (Figure 4.4). All β values were estimated on the $\log_{10}$ scale.

Across stages, EBI effects were stronger for differentiation than for proliferation, except at the proerythroblast (ProE) stage, where proliferation showed greater dependence on EBI support. At later stages (BasoE, PolyE), weaker proliferation modulation is consistent with a niche programme that prioritises maturation over expansion.

To test whether all eight β parameters were necessary for model performance, we applied L1 (LASSO) regularisation during fitting. None of the β terms were shrunk to zero, indicating that EBI-mediated regulation contributes across multiple erythroid checkpoints.

Overall, the fitted parameters support a model in which EBIs primarily accelerate erythroid maturation, consistent with experimental evidence that EBIs act as maturation-supporting niches throughout erythropoiesis[6,10].

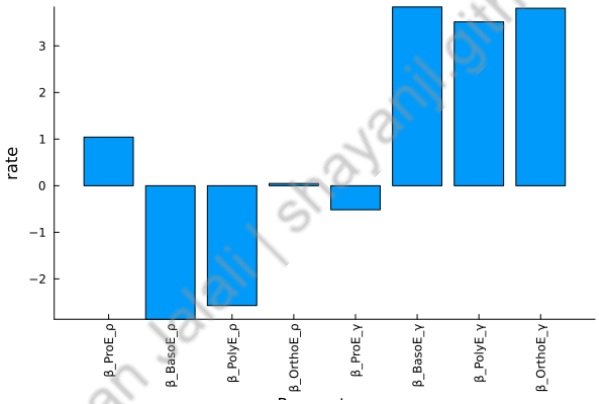

Figure 4.4: Estimated $\log_{10}$-scale strengths of EBI influence (β parameters) on proliferation (ρ) and differentiation (γ) rates. Differentiation effects are consistently stronger, except at the ProE stage. LASSO-regularised fitting confirmed that all β terms contribute to model performance.

Together, the modelling results indicate that EBIs function mainly as maturation-supporting niches. The next section therefore examines transcriptional changes in nurse macrophages under AML to probe molecular correlates of niche dysfunction.

4.3 Transcriptomic Analysis of Nurse Cells in AML

To investigate mechanisms underlying nurse cell and erythroblastic island (EBI) disruption in AML, we performed transcriptomic profiling of F4/80$^+$VCAM-1$^+$CD169$^+$ nurse macrophages sorted from the bone marrow of healthy mice and AML-infiltrated mice (11.8%, 37.8%, and 69.8% infiltration). This analysis was used to identify molecular changes associated with niche dysfunction and to relate them to the model-derived hypotheses.

Functional enrichment analysis

Transcriptomic profiling indicated alterations in immune-related and niche-associated pathways in AML-exposed nurse cells (data not shown). Canonical EBI-associated genes (e.g., *Maea*, *Vcam1*, *Dnase2a*) remained detectable, suggesting partial retention of EBI identity in the surviving nurse macrophage population. In contrast, transcriptional signatures were consistent with reduced activity of survival- and proliferation-associated programmes, including MYC-related regulation (data not shown). Given the established role of MYC in macrophage viability, these trends may contribute to progressive nurse cell loss during AML.

Integration with modelling

The model predicts that attenuation of extrinsic survival cues, including M-CSF–mediated signalling, destabilises EBIs and drives nurse cell attrition. The transcriptomic trends observed in AML-associated nurse cells were compatible with reduced survival-associated programmes, supporting this mechanism (data not shown). These results provide molecular context for the niche-failure dynamics captured by the model.

The following section benchmarks global sensitivity analysis methods under controlled test problems before applying them to the erythropoiesis model.

4.4 Comparison of GSA Methods for Different Sample Sizes and Problem Dimensions

Global sensitivity analysis (GSA) was used to identify influential parameters without repeatedly solving the full ODE system. We benchmarked surrogate-based Sobol indices via Polynomial Chaos Expansion (PCE) against variance-based, gradient-free alternatives to characterise accuracy–cost trade-offs on low- and moderate-dimensional test problems before applying GSA to the erythropoiesis model[164,166]. In parallel, VARS and its extensions (GVARS and DVARS) were implemented in Julia (`VariogramAnalysis.jl`) as a complementary framework for high-dimensional screening under limited computational budgets[167].

4.4.1 Sobol–G problem

The Sobol–G function is a standard benchmark for sensitivity analysis because analytical indices are available and the problem scales naturally with dimension, enabling controlled evaluation of method performance[164].

On this benchmark, PCE-based Sobol indices converged rapidly and produced deterministic (noise-free) sensitivity estimates from surrogate coefficients, consistent with the advantages of polynomial surrogates for smooth response surfaces[166]. VARS/IVARS were computed using `VariogramAnalysis.jl`[167] and validated against a Python reference implementation, with bootstrap resampling used to quantify uncertainty; agreement was observed across repeated sampling designs.

We then benchmarked Sobol, eFAST, PCE (degree 2), and VARS across multiple dimensions ($d = 3, 10, 30, 40$) and computational budgets ($N = 5000, 50\,000, 100\,000$). Each

configuration was repeated 20 times, and performance was summarised using mean absolute error (MAE) relative to analytical indices, with error bars showing ±1 standard deviation.

Results are summarised in Figure 4.5. Classical Monte Carlo Sobol estimators converged slowly in this setting, whereas PCE remained stable across dimensions (with error limited by the fixed polynomial degree)[166]. eFAST showed good accuracy at moderate dimensions, consistent with spectral variance-based estimation[162,165]. VARS consistently improved upon classical Sobol estimation and approached eFAST performance, particularly at lower dimensions and larger budgets[167].

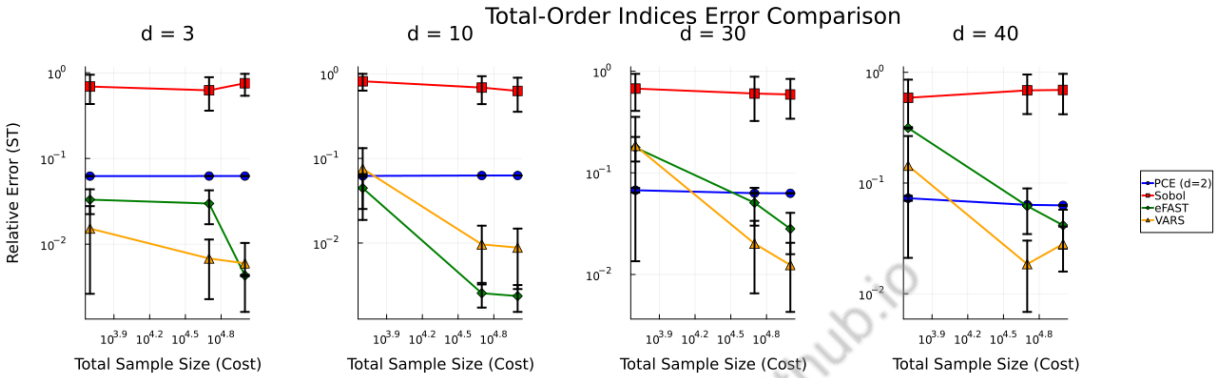

Figure 4.5: Comparison of Sobol, eFAST, PCE, and VARS on the Sobol–G benchmark function at increasing dimensionality ($d = 3, 10, 30, 40$) and sample sizes ($N = 5000, 50\,000, 100\,000$). Each point represents the mean absolute error (MAE) over 20 repeats, with error bars showing ±1 standard deviation. VARS and eFAST consistently outperformed Sobol, while PCE remained stable but limited by polynomial order.

In summary, the Sobol–G benchmark indicates that VARS and eFAST are computationally efficient alternatives to classical Sobol estimators under constrained budgets, with VARS providing a practical balance between accuracy and robustness[162,165,167]. Validation against a Python reference implementation further supports the reliability of the Julia implementation developed in this work.

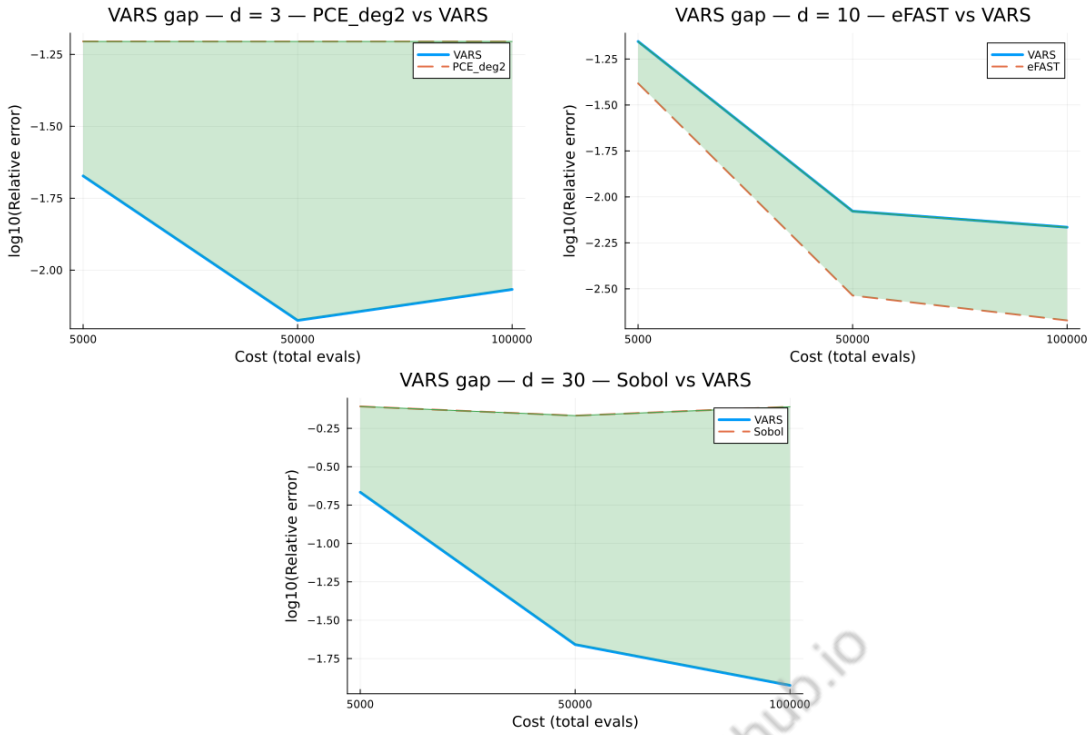

Figure 4.6: Representative VARS gap plots comparing relative error ($\log_{10}$ scale) of VARS against baseline methods across different dimensionalities. (**Top left**) VARS vs PCE at $d = 3$: PCE achieves consistently lower error in smooth, low-dimensional problems. (**Top right**) VARS vs eFAST at $d = 10$: both methods converge to similarly low error, demonstrating efficiency in moderate dimensions. (**Bottom**) VARS vs Sobol at $d = 30$: VARS outperforms Sobol by more than an order of magnitude, highlighting its robustness under higher dimensionality. Full sets of gap plots for all dimensions and methods are provided in Appendix 6.

4.4.2 Exponential Decay Problem

The exponential decay model provides a biologically motivated yet analytically tractable benchmark. Because the response is smooth and exhibits weak interactions, PCE produced stable first- and total-order indices using substantially fewer model evaluations than direct Monte Carlo estimators, consistent with the expected efficiency of accurate surrogate models[166,176]. In parallel, VARS indicated low sensitivity of the response to the initial condition and rate parameter in this setting, providing a useful baseline before analysing more complex ODE systems[167].

To evaluate performance systematically, Sobol, PCE, eFAST, and VARS were compared under matched computational budgets across increasing dimensionality ($d = 3, 10, 20, 40$)[164,177]. Each configuration was repeated 20 times, and the mean absolute error (MAE) of total-order indices was computed against analytical reference values. The results are summarised in Figure 4.7. PCE achieved the lowest error (on the order of 10^{-4}) across all dimensions and budgets, reflecting its advantage for smooth, low-interaction problems. Classical Sobol estimators converged more slowly, with error increasing as dimensionality grew. eFAST performed well at moderate dimensions but did not complete reliably at $d = 40$ under the distributed execution setup. VARS produced stable estimates across all dimensions but showed larger MAE in this benchmark, consistent with its intended use as

a robust screening method rather than a high-precision variance-decomposition estimator for smooth, low-interaction responses[167].

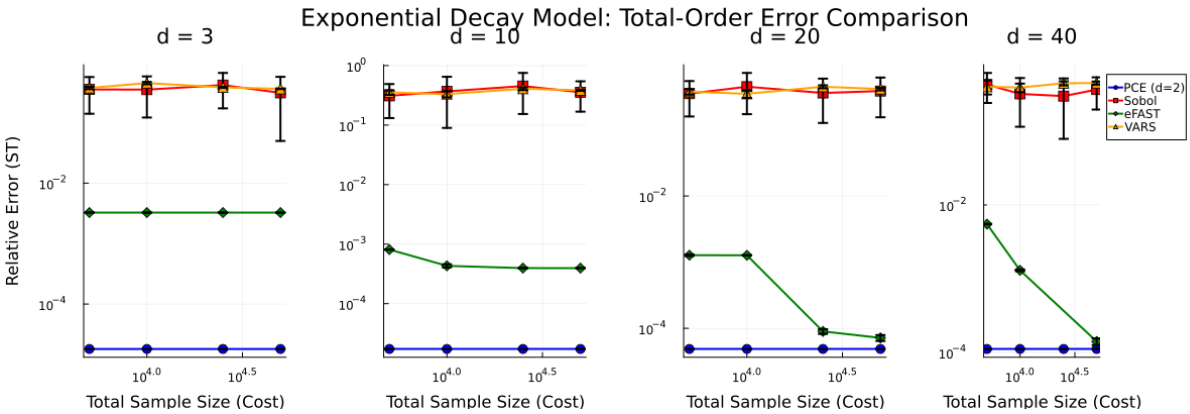

Figure 4.7: Comparison of total-order index error across Sobol, PCE, eFAST, and VARS on the exponential decay model at increasing dimensionality ($d = 3, 10, 20, 40$). PCE maintained consistently low error across all cases, Sobol required large samples to converge, eFAST did not complete reliably at $d = 40$ under our execution setup, and VARS remained stable but less accurate in absolute MAE.

Taken together, these results support PCE as an efficient and accurate approach for global sensitivity analysis in smooth dynamical systems, while highlighting VARS as a complementary method that provides robust screening and ranking under constrained budgets.

4.4.3 APMC-based Sensitivity Analysis

As an additional global approach, Adaptive Population Monte Carlo (APMC) was used to quantify parameter influence within a Bayesian sampling framework[159,178]. APMC iteratively refines a population of parameter samples, enabling efficient exploration of nonlinear and high-dimensional parameter spaces[178,179]. Parameter influence was summarised using the inverse posterior covariance matrix, which was interpreted as a proxy for how strongly each parameter is constrained by the experimental data.

Figure 4.8 presents the ranked influence values on a logarithmic scale. The strongest contributors were the red blood cell decay rate (δ_{R}), the differentiation transition from basophilic to polychromatic erythroblasts ($\gamma_{\mathrm{BasoE}\to\mathrm{PolyE}}$), and nurse-cell related parameters (ρ_{Nurse}, ρ_{MCSF}). These results highlight erythrocyte turnover and nurse-cell mediated support as key determinants of erythropoiesis under leukaemic stress.

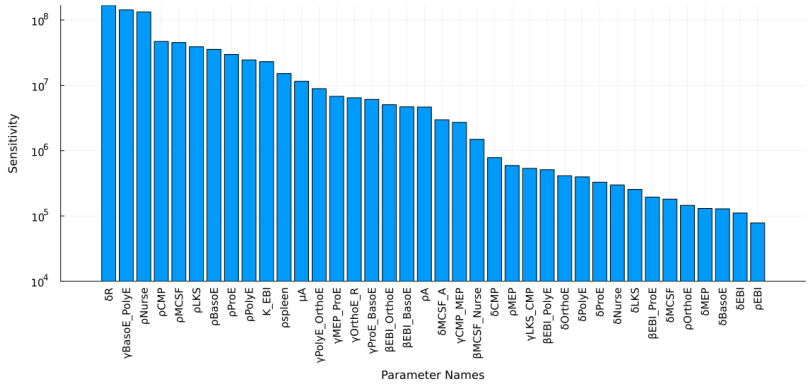

Figure 4.8: APMC-based analysis showing ranked parameter influence values on a logarithmic scale. The red blood cell decay rate (δ_{R}), the BasoE $\rightarrow$ PolyE differentiation transition ($\gamma_{\mathrm{BasoE}\rightarrow\mathrm{PolyE}}$), and nurse-cell related parameters (ρ_{Nurse}, ρ_{MCSF}) emerge as the most influential drivers of model behaviour, highlighting erythroid turnover and nurse-cell support as critical constraints under leukaemic stress.

Taken together, the PCE, VARS, and APMC results provide complementary insights. PCE achieved rapid convergence on smooth, low-interaction systems; VARS offered efficient total-order screening under limited sample sizes; and APMC highlighted biologically critical parameters in the full erythropoiesis model through a posterior constraint-based perspective. Collectively, these analyses reinforce the centrality of nurse-cell support and M-CSF availability as leverage points in AML-associated erythropoietic failure.

This comparative evaluation establishes the methodological basis for applying global sensitivity analysis to the erythropoiesis model in the subsequent results.

4.5 OAT Sensitivity Analysis of Erythropoiesis Model

As a baseline, we applied classical One-At-a-Time (OAT) sensitivity analysis. This method perturbs one parameter while holding all others fixed, approximating single-factor experimental perturbations and identifying parameters with strong local effects. While informative for direct influences, OAT does not capture parameter interactions (e.g., nurse-cell dynamics coupled to EBI-mediated transitions). This limitation motivated our reliance on global sensitivity indices for final parameter ranking (see Section 4.6).

4.5.1 Parameter Sensitivity Curves

Figure 4.9 shows representative OAT sensitivity curves for the most influential parameters under three perturbation regimes: $\pm 10\%$, $\pm 50\%$, and the full prior range. The x-axis corresponds to the parameter value on a $\log_{10}$ scale, and the y-axis represents the squashed error (a bounded, normalised model–data discrepancy metric).

At the $\pm 10\%$ range, parameters such as $\gamma_{\mathrm{ProE}\rightarrow\mathrm{BasoE}}$, ρ_{ProE}, β_{ProE}, ρ_{Nurse}, and δ_{Nurse} showed steep error responses, indicating strong local influence on erythroblast proliferation and nurse-cell survival. At wider ranges ($\pm 50\%$ and full range), parameters related to AML dynamics (δ_{A}, ρ_{A}) and M-CSF signalling ($\beta_{\mathrm{MCSF\_Nurse}}$, ρ_{MCSF}) emerged as additional

contributors, reflecting nonlinear amplification of model discrepancy when parameters deviate far from nominal values[159].

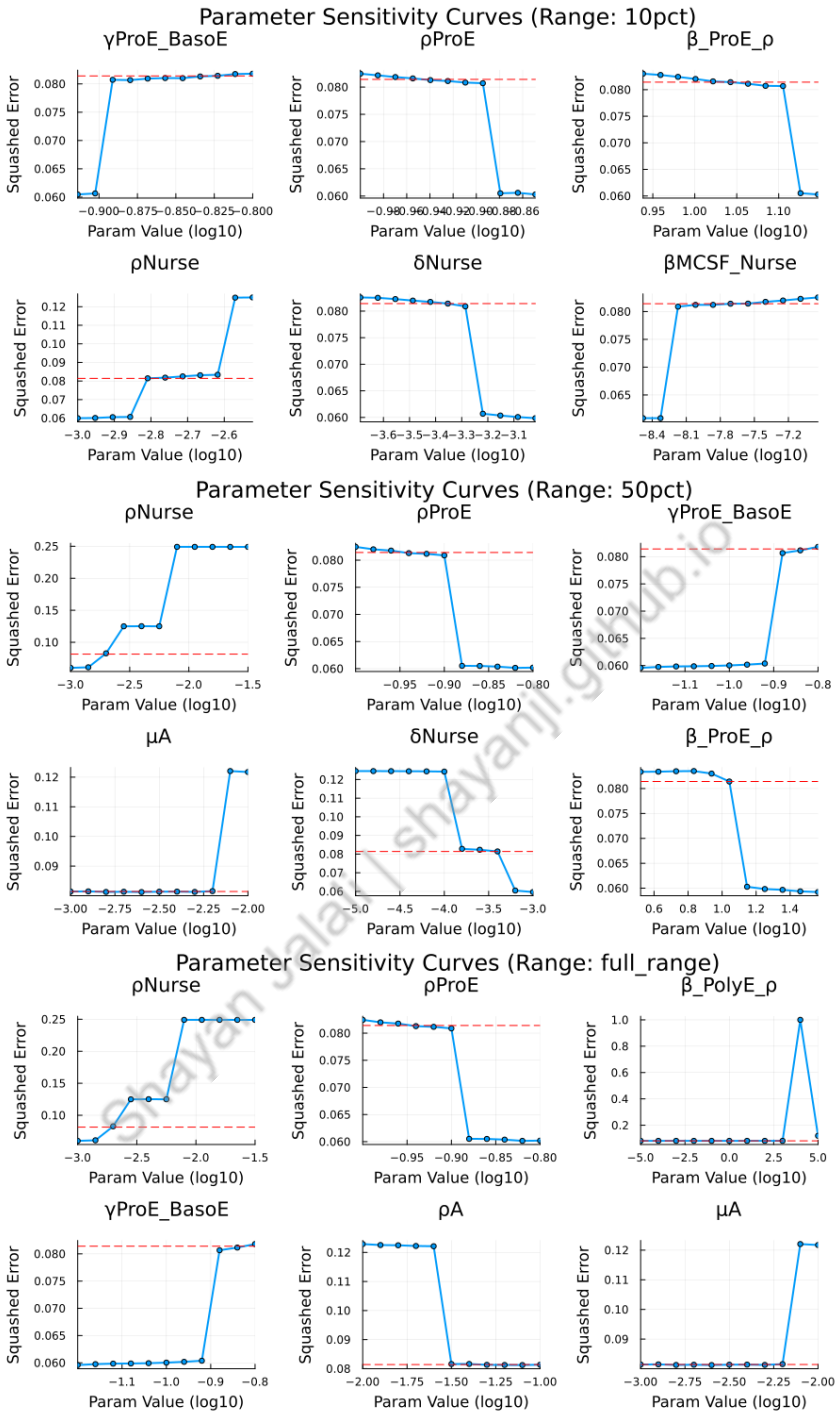

Figure 4.9: Representative OAT sensitivity curves showing squashed error as a function of log-scaled parameter values. Panels display the top six most sensitive parameters at three perturbation scales: (Top) ±10%, (Middle) ±50%, and (Bottom) full prior range. Steep slopes correspond to parameters exerting strong local influence on erythropoiesis under AML stress.

4.5.2 Top Parameter Rankings

Figure 4.10 summarises the top 15 most influential parameters identified under each perturbation range. Across all ranges, the nurse-cell production rate (ρ_{Nurse}), proerythroblast proliferation (ρ_{ProE}), and the ProE→BasoE transition rate ($\gamma_{\text{ProE}\to\text{BasoE}}$) consistently ranked among the most sensitive parameters, highlighting their central role in coupling erythroid amplification to macrophage-supported niche function.

At the narrow perturbation range (±10%), sensitivity was dominated by lineage-intrinsic differentiation and proliferation processes. As the perturbation range widened (±50% and full prior range), parameters governing AML growth (δ_{A}, ρ_{A}) and M-CSF-related signalling gained prominence, indicating that leukaemic disruption becomes increasingly apparent when exploring broader deviations from the calibrated baseline.

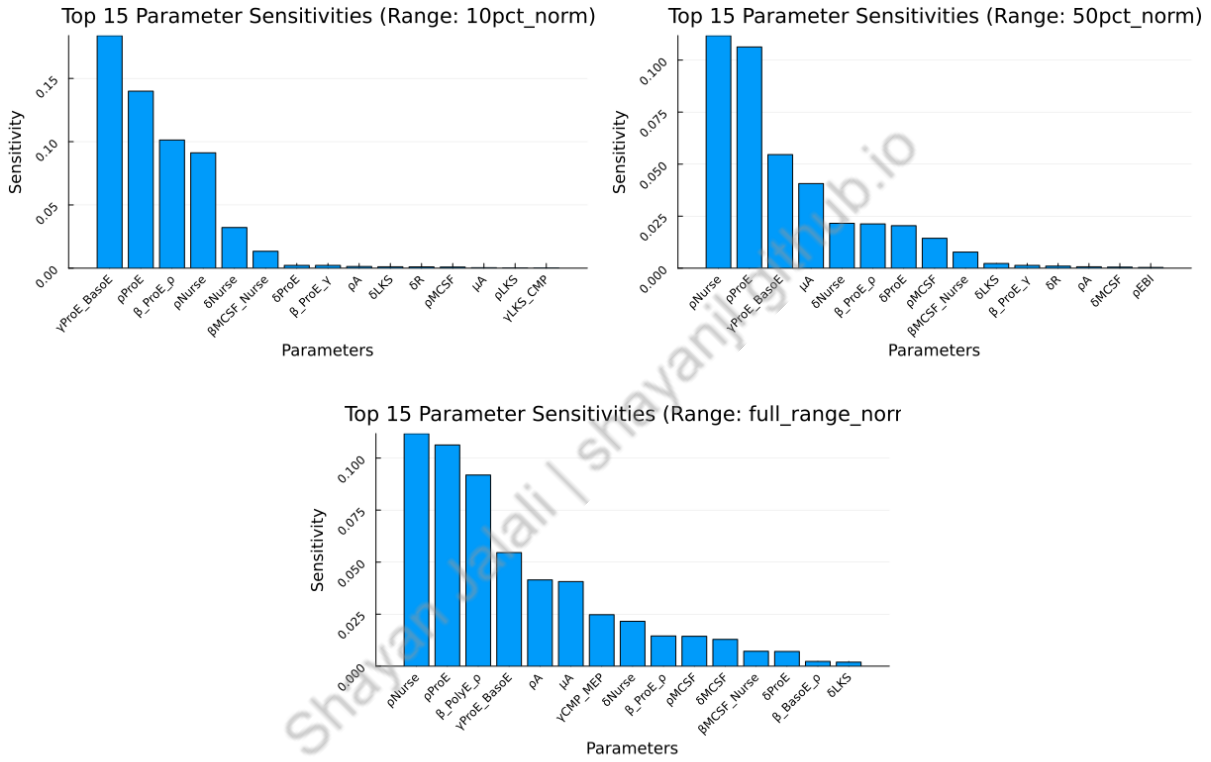

Figure 4.10: Top 15 parameter sensitivities ranked by the normalised OAT index. (Top Left) ±10%, (Top Right) ±50%, and (Bottom) full prior range. Nurse-cell turnover ($\rho_{\text{Nurse}}, \delta_{\text{Nurse}}$), proerythroblast proliferation (ρ_{ProE}), and erythroblast differentiation ($\gamma_{\text{ProE}\to\text{BasoE}}, \beta_{\text{ProE}}$) consistently emerge as key drivers of system dynamics. AML-related parameters ($\delta_{\text{A}}, \rho_{\text{A}}$) and M-CSF signalling components gain prominence under larger perturbations.

4.5.3 Interpretation

OAT sensitivity analysis indicates that erythroblast differentiation and nurse-macrophage survival are tightly constrained processes, as small perturbations in associated parameters produce measurable deviations in erythropoietic output. Under broader perturbations, the analysis further emphasises the disruptive contribution of AML proliferation and impaired M-CSF signalling, consistent with a niche-mediated mechanism of erythropoietic

suppression and a therapeutic rationale centred on preserving nurse-cell support and macrophage survival cues.

Overall, OAT provides an interpretable baseline quantification of single-parameter influence that complements global methods. Whereas global approaches capture interaction structure and higher-order effects, OAT confirms the biological plausibility of key regulatory processes and offers an intuitive point of comparison when interpreting more comprehensive sensitivity indices.

These OAT results therefore motivate a transition to global sensitivity analysis to quantify interaction-driven influences on erythroid output and to obtain variance-based parameter rankings.

4.6 Global Sensitivity Analysis of the Erythropoiesis Model

To investigate parameter influence on simulation outcomes while controlling computational cost, we employed a global sensitivity analysis (GSA) strategy based on a Polynomial Chaos Expansion (PCE) surrogate model[176,180]. Unlike local perturbation methods, this framework decomposes output variance into first-order (direct), higher-order (interaction), and total effects for each parameter. To focus on experimentally tractable erythropoiesis and niche mechanisms rather than intrinsic AML growth kinetics, we excluded AML-specific growth parameters (ρ_{A}, δ_{A}) and varied the remaining 39 parameters within a $\pm 10\%$ window around the best-fit set obtained by xNES optimisation.

4.6.1 Polynomial Chaos Expansion Method Results

We constructed a degree-3 Polynomial Chaos Expansion (PCE) surrogate to approximate the mapping from 39 input parameters to the models fold-change outputs. Inputs were scaled to $[0, 1]$ and sampled uniformly within a $\pm 10\%$ perturbation window. Sobol first-order, second-order, and total-order sensitivity indices were computed analytically from the fitted PCE coefficients, avoiding Monte Carlo estimation and reducing sampling noise.

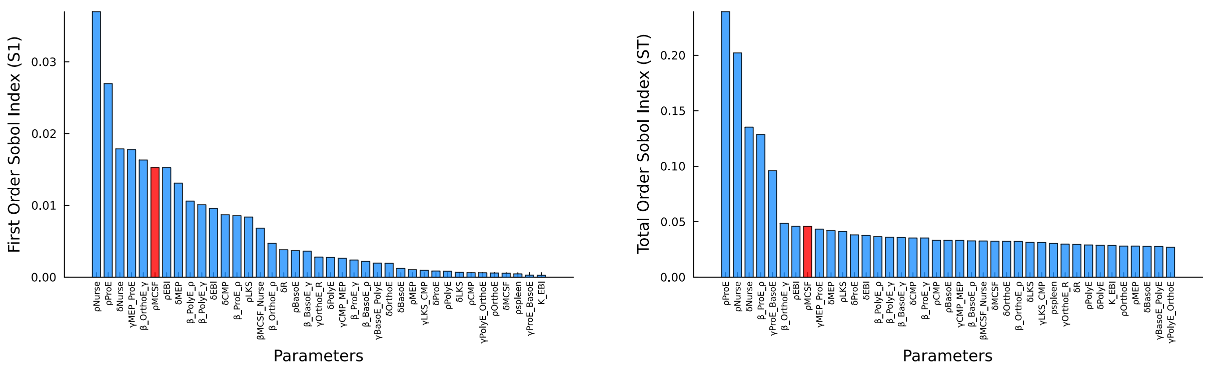

Figure 4.11: Global sensitivity analysis results for the reduced parameter set (excluding intrinsic AML parameters). Left: first-order Sobol indices (S_j). Right: total-order indices (S_{T_j}). The baseline M-CSF production rate (ρ_{MCSF}) is highlighted in red.

The PCE–Sobol results identified nurse-cell production (ρ_{Nurse}) and proerythroblast proliferation (ρ_{ProE}) as dominant contributors to output variance, together with nurse-cell decay (δ_{Nurse}) and early transition rates ($\gamma_{\text{MEP}\to\text{ProE}}$). Notably, the baseline M-CSF production rate (ρ_{MCSF}) emerged as both influential and experimentally tractable, motivating M-CSF supplementation as a therapeutic axis for stabilising nurse-cell support.

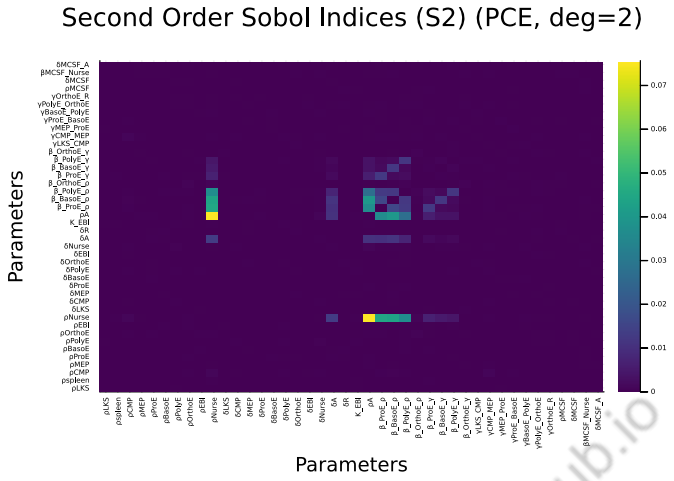

Figure 4.12: Second-order Sobol indices (S_{ij}) computed using a degree-2 Polynomial Chaos Expansion (PCE) surrogate. The heatmap highlights pairwise parameter interactions within the reduced parameter set. Brighter regions correspond to stronger interactions, with notable effects observed between nurse-cell parameters (ρ_{Nurse}, δ_{Nurse}) and early erythropoiesis regulators (ρ_{ProE}, $\gamma_{\text{MEP}\to\text{ProE}}$).

Second-order indices from the degree-2 PCE surrogate revealed a limited number of prominent pairwise interactions, consistent with the low-order approximation. The strongest interactions involved nurse-cell production coupled to proerythroblast proliferation and MEP→ProE differentiation, while weaker interaction structure suggested additional contributions involving M-CSF–dependent support of nurse cells. Together, these results reinforce the central role of nurse-cell turnover and M-CSF signalling in AML-associated niche disruption and demonstrate that low-order interaction terms capture key mechanisms underlying erythropoietic failure.

4.6.2 VARS Method Results

VARS (Variogram Analysis of Response Surfaces) provided a complementary screening analysis, and its parameter rankings were consistent with the PCE–Sobol results (Table 4.1; Fig. 4.11). Nurse-cell turnover and M-CSF availability emerged as dominant drivers of model output, with additional sensitivity concentrated in transitions feeding the ProE compartment[167].

VARS achieved comparable ranking stability using approximately 50–60% of the function evaluations required by standard variance-decomposition estimators in our benchmarking setup, which is advantageous when ODE simulations are costly.

Across benchmark problems spanning $d = 3, 10, 20, 40$, VARS remained robust under matched evaluation budgets (typical error $\approx$ 0.01–0.10). By contrast, classical Sobol

and FAST-family approaches generally require increasing sample sizes as dimensionality grows[162,164].

Overall, VARS is well suited for high-dimensional screening under constrained budgets, whereas PCE is preferable when full variance decomposition (S_1, S_2, S_T) is required[166,167].

Method	Sensitivity Indices	Optimal Use Case	Efficiency	Computational Cost	Model Complexity Suitability
VARS	S_T only	High dimensions, limited budget	Excellent	Low-to-Moderate	High-dimensional, screening
PCE (deg. 2)	S_1, S_2, S_T	Complete analysis	Good	Moderate	Nonlinear, complex models
eFAST	S_T, partial S_1	Low/medium dimensions	Good	Moderate-to-High	Moderate complexity
Sobol	S_1, S_2, S_T	Standard benchmark	Poor scaling	High	Moderate-to-High

Table 4.1: Comparison of VARS, PCE, eFAST, and Sobol across sensitivity indices, efficiency, computational cost, and model complexity suitability.

Collectively, these global analyses quantify how variation in niche support and cytokine feedback propagates to erythroid output, enabling direct comparison with the local OAT results presented next.

4.7 Comparison of GSA and OAT Sensitivity Analysis Findings

Comparing one-at-a-time (OAT) and global (PCE–Sobol, VARS) sensitivity analyses yielded complementary insights into erythropoiesis under leukaemic stress. Across methods, parameters governing nurse-cell dynamics and macrophage-associated cytokine support repeatedly emerged as influential, although their relative ranking depended on whether interaction effects were captured[162,164,167].

Global analyses highlighted the baseline M-CSF production rate (ρ_{MCSF}) and nurse-cell turnover parameters (ρ_{Nurse}, δ_{Nurse}) as major drivers of output variability, consistent with interaction-mediated influence propagated through erythroblastic islands (EBIs). By contrast, OAT perturbations emphasised parameters with strong local effects around the calibrated baseline and can under-rank factors whose impact is expressed primarily through multi-parameter coupling[160,162].

4.8 Therapeutic Implications: Targeting Nurse Cells via M-CSF to Restore Erythropoiesis with Limited AML Suppression

Across both OAT and global sensitivity analyses, the baseline M-CSF production rate (ρ_{MCSF}) and nurse-cell production rate (ρ_{Nurse}) consistently ranked among the most influential parameters. This points to nurse macrophage support as a key bottleneck for maintaining erythropoiesis under leukaemic stress and identifies M-CSF signalling as a tractable lever for niche stabilisation.

Because M-CSF regulates macrophage survival and maintenance and can be administered exogenously[46,98,99], the sensitivity results provide a rationale for investigating M-CSF supplementation as a strategy to counter AML-associated erythropoietic failure. More broadly,

macrophage-directed approaches (e.g., CSF1R-axis modulation or pro-phagocytic strategies) have shown therapeutic activity in other malignancies[181], although their relevance to preserving erythropoiesis in AML remains less well established.

Consistent with this interpretation, the model predicts that nurse-cell decline accompanies erythroblastic island (EBI) collapse as AML burden increases, implicating niche disruption as a major contributor to erythroid failure[10,20,108]. Simulations further indicate that M-CSF supplementation can rescue nurse-cell abundance and partially restore erythropoiesis, while exerting only limited direct suppression of AML growth. Thus, M-CSF primarily emerges as a niche-stabilising intervention that improves erythroid output in the presence of leukaemic stress rather than as a direct anti-leukaemic therapy.

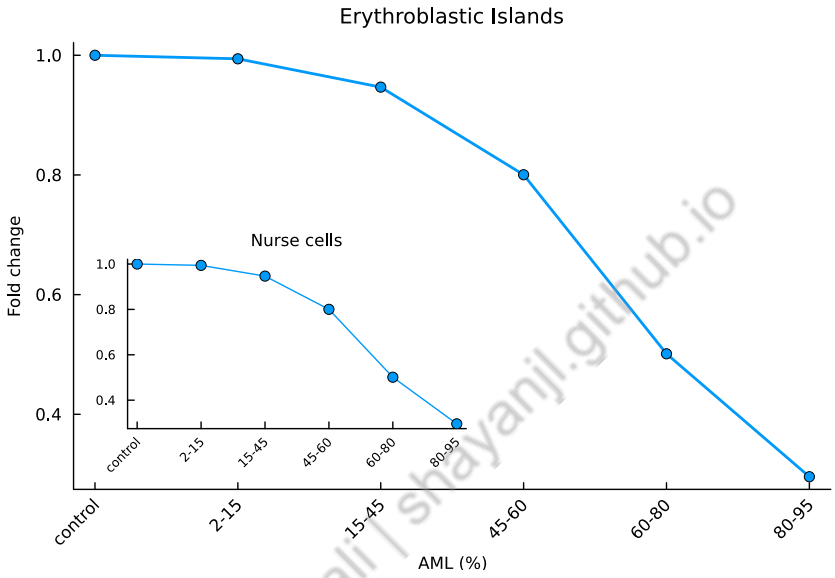

Figure 4.13: Model predictions showing progressive collapse of erythroblastic islands (EBIs) with increasing AML burden, accompanied by a decline in nurse-cell populations (inset). These results highlight the coupled vulnerability of EBIs and nurse cells under leukaemic stress, motivating therapeutic strategies aimed at stabilising nurse-cell function.

Model-Based Predictions

Exogenous M-CSF administration was represented by adding a time-dependent, pulsed production term to the M-CSF equation. The resulting schedule (Fig. 4.15) was used to examine how injection amplitude (A_{MCSF}) alters erythropoiesis and AML burden. The model was not calibrated to injection pharmacokinetics; therefore, to reflect uncertain bone marrow bioavailability, a broad range of A_{MCSF} values was explored.

Across this range, simulations predicted increased nurse-cell abundance after M-CSF dosing, with partial rescue of erythropoiesis and only modest changes in leukaemic burden (Fig. 4.15). Rescue was strongest in progenitor and intermediate erythroid stages (I–V), whereas the mature RBC pool changed more gradually over the simulated time horizon, consistent with its longer lifespan. At the highest simulated doses, the model also predicted a small reduction in AML burden, a trend not observed experimentally.

Model-Guided Experimental Observations

Based on the computational predictions, recombinant M-CSF was tested *in vivo* in the MLL-AF9 AML mouse model as an exploratory intervention. M-CSF supplementation was associated with increased nurse-cell abundance and a partial improvement in erythropoiesis, without an apparent change in overall AML burden (data not shown). Effects were most evident in early erythroid stages, including proerythroblasts (I), basophilic (II), and polychromatic (III) populations, whereas orthochromatic erythroblasts (IV) and leukaemic infiltration appeared largely unchanged. These observations support the interpretation that M-CSF primarily stabilises the erythropoietic niche rather than exerting direct anti-leukaemic activity.

Together, the computational and experimental findings support M-CSF as a niche-targeted strategy for mitigating AML-associated erythropoietic failure and justify further investigation in more rigorously powered studies.

Therapeutic Insights

Across simulation scenarios, pulsed M-CSF administration improved EBI integrity and nurse-cell abundance, with little change in AML dynamics over the simulated time horizon (Figure 4.14). The erythropoietic response scaled with injection amplitude: increasing A_{MCSF} progressively increased nurse cells and early erythroid progenitors, whereas AML levels showed only minor changes (Figure 4.15). This amplitude-dependent rescue aligns with the global sensitivity analysis, which ranked ρ_{MCSF} among the most influential parameters shaping model behaviour. Overall, the simulations suggest that M-CSF acts primarily as a niche-stabilising intervention that can restore erythropoietic function under leukaemic stress, rather than as a direct anti-leukaemic strategy.

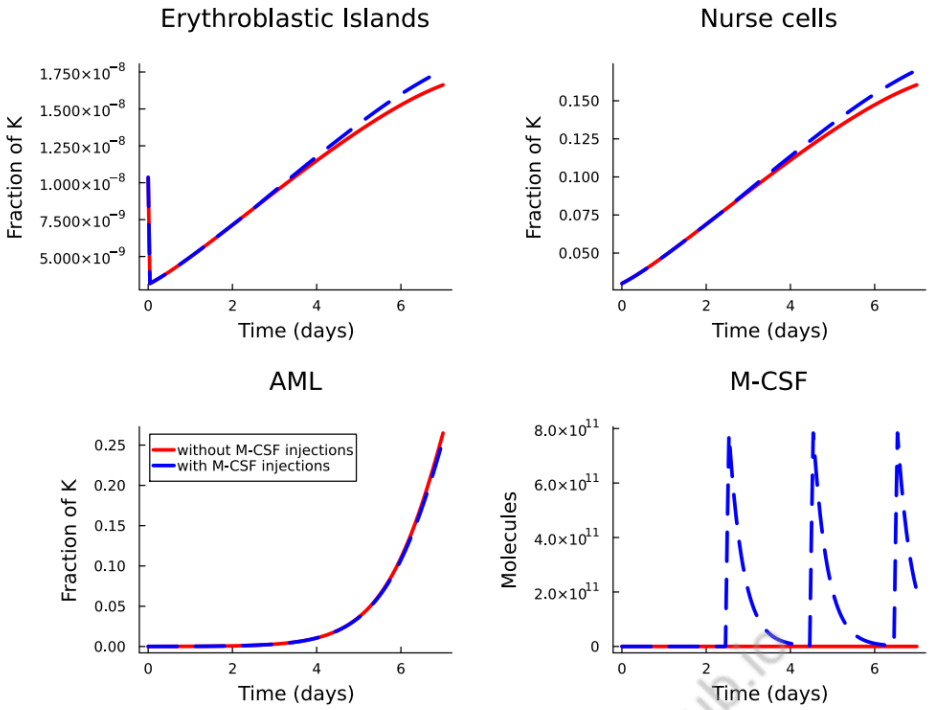

Figure 4.14: Time-course dynamics of M-CSF intervention. Red lines show trajectories without M-CSF injections, and blue lines show trajectories with pulsed M-CSF administration. Top: Erythroblastic islands (left) and nurse cells (right) both increase with M-CSF injections, reflecting rescue of the erythropoietic niche. Bottom: AML dynamics (left) remain largely unchanged, indicating limited direct anti-leukaemic effects, while the injection schedule is captured by transient M-CSF peaks (right).

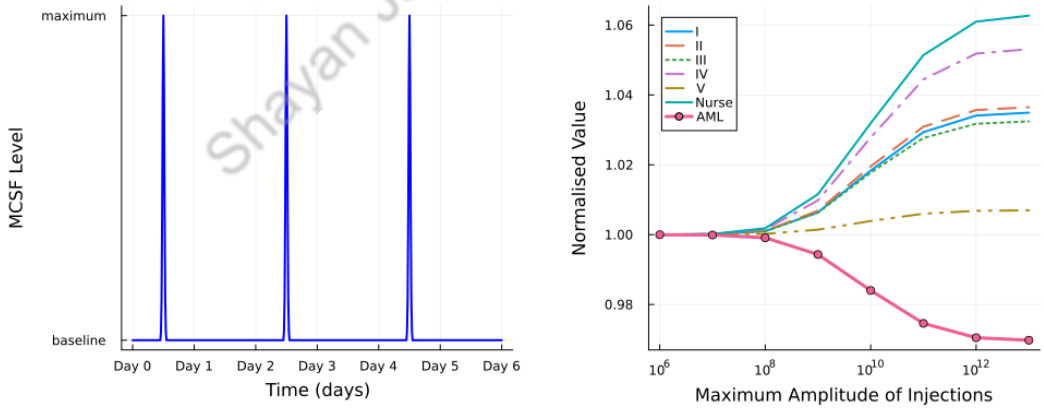

Figure 4.15: Impact of M-CSF injections on erythropoiesis and AML. Left: pulsed M-CSF injection schedule over seven days, with baseline and maximum levels indicated. Right: model-predicted dose–response across a wide range of injection amplitudes (A_{MCSF}). Nurse cells and early erythroid populations (I–V) show progressive rescue with increasing M-CSF amplitude, whereas AML levels are only modestly reduced. These results highlight that M-CSF primarily stabilises the erythropoietic niche rather than directly suppressing AML.

Identifying macrophage-centred and cytokine-based regulatory axes provides a framework

for testing whether combined interventions can restore erythroid maturation more effectively than single-agent treatments.

4.9 Combined Therapeutic Strategies: M–CSF and Anti–IL-6

Motivated by the global sensitivity analysis implicating the nurse-cell/M–CSF axis and evidence that IL-6 can impose an inflammatory blockade on erythropoiesis[113–115], we evaluated a two-agent intervention combining exogenous M–CSF with IL-6 neutralisation[46]. We simulated short, pulsed courses (0–3 injections per agent) under two dosing sequences: *M–CSF first, anti–IL-6 second* and *anti–IL-6 first, M–CSF second*. Figure 4.16 summarises fold changes (relative to no treatment) for AML, erythroid compartments I–V, and nurse cells across the 4×4 grid of injection counts for each sequence.

Across both sequences, ordering affected AML outcomes, although the overall AML effect remained modest. AML burden decreased most when *anti–IL-6 was administered first and M–CSF added afterwards*; under this ordering, increasing M–CSF injections produced a monotone reduction in AML. In contrast, when *M–CSF was given first*, AML changes remained limited even after anti–IL-6 was added. This is consistent with the idea that relieving inflammatory suppression before augmenting niche support more effectively constrains leukaemic expansion over the simulated time window.

Nurse-cell abundance was driven predominantly by M–CSF and showed only weak dependence on anti–IL-6 dose. In both sequences, nurse-cell fold changes increased strongly along the M–CSF injection axis, consistent with M–CSF acting as the principal regulator of nurse-macrophage survival and maintenance.

The largest erythroid rescue occurred in intermediate stages (II–IV), where combined therapy produced substantial fold increases. Two effects were robust across the design space: anti–IL-6 alleviated inflammatory inhibition of erythropoiesis, and M–CSF further amplified rescue by expanding nurse-cell support. Synergy was strongest when anti–IL-6 preceded M–CSF, consistent with IL-6 blockade unmasking maturation support that is then strengthened by increasing nurse-cell abundance.

By contrast, stage I and the mature RBC pool (V) exhibited comparatively small changes. This behaviour is consistent with the models lifespan structure: early progenitors are upstream of the main AML-sensitive bottlenecks, whereas mature RBCs turn over slowly, so short intervention courses propagate only weakly to compartment V within the simulated horizon.

Mechanistically, these simulations reinforce a niche-centric interpretation consistent with the PCE–Sobol and APMC analyses: anti–IL-6 reduces inflammatory inhibition of erythropoiesis, while M–CSF expands nurse cells that stabilise EBIs and preferentially support differentiation.

From a translational perspective, the model predicts that the combination regimen primarily improves erythroid recovery, whereas effects on AML burden are secondary over short time horizons. Accordingly, near-term endpoints are more likely to reflect erythroid output (e.g., reticulocyte recovery or reduced transfusion requirement) than major reductions in leukaemic burden, and longer follow-up or repeated cycles may be required for benefits to

propagate to the mature RBC compartment.

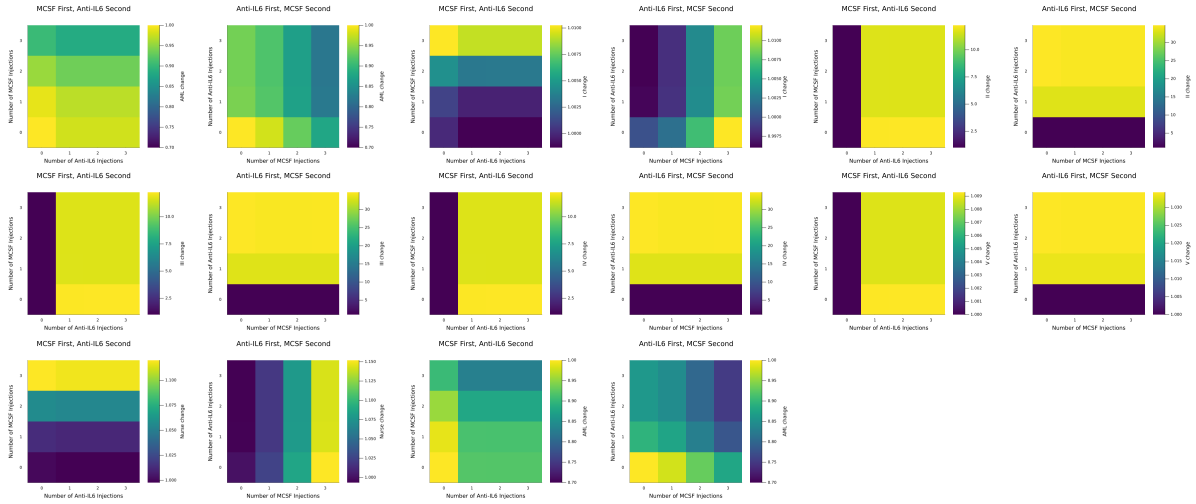

Figure 4.16: Combined therapy design space. Heatmaps report fold change relative to baseline for AML, erythroid compartments I–V, and nurse cells under two sequences: *M–CSF first, anti–IL-6 second* (left column within each panel) and *anti–IL-6 first, M–CSF second* (right column within each panel). Axes denote the number of injections (0–3) in each course. Cooler colours in the AML panel indicate lower leukaemic burden; warmer colours in I–V and nurse panels indicate larger increases. The strongest and most consistent improvements occur when anti–IL-6 precedes M–CSF, with nurse cells and intermediate stages (II–IV) showing the largest gains.

Overall, the combination modelling highlights synergistic effects between macrophage-directed niche support and cytokine modulation, motivating broader exploration of secondary targets that may reinforce erythroid rescue pathways.

Scope and translational context. These simulations should be interpreted as hypothesis-generating rather than predictive of clinical efficacy. The model identifies plausible mechanisms by which exogenous M–CSF may stabilise erythroid niches and how IL-6 blockade may complement this effect; however, quantitative outcomes depend on unmodelled variables including pharmacokinetics, cytokine clearance, systemic inflammatory feedback, and inter-individual variability. Accordingly, while the simulated trends are consistent with observations in murine models, definitive conclusions about therapeutic benefit require in vivo and translational studies that explicitly test these combined interventions under controlled conditions.

4.10 Additional Potential Targets for Future Experimental Investigation

Beyond M-CSF–mediated niche support, the combined experimental and computational findings suggest additional regulatory axes that may be targeted to improve erythropoiesis and reduce AML-associated niche dysfunction. AML was associated with loss of nurse macrophages, depletion of erythroblastic islands (EBIs), and transcriptomic signatures consistent with impaired survival pathways, including reduced MYC- and KLF1-associated

transcriptional programmes[182]. Altered adhesion phenotypes were also observed, including changes in CD169 and VCAM-1 expression. These results motivate three complementary classes of targets for future investigation.

First, strengthening mesenchymal stromal cell (MSC)–derived support of macrophage survival, including the MSC–M-CSF axis, may help preserve nurse macrophage abundance and maintain EBI integrity under leukaemic stress by restoring local cytokine availability. Second, modulation of adhesion-dependent EBI assembly may stabilise macrophage–erythroblast contact and niche architecture. Candidate mechanisms include ICAM4/$\alpha 4\beta 1$–VCAM-1 interactions[183] and MAEA-dependent erythroblast–macrophage coupling[20]. Third, reinforcing nurse-cell survival programmes regulated by MYC and KLF1 may counter AML-associated suppression of macrophage-supportive states and thereby sustain erythroid maturation support.

Together, these targets provide a framework for future studies aimed at sustaining erythroid maturation under leukaemic stress.

4.11 Enhanced Basophilic Erythroblast Production Strongly Attenuates AML-induced Disruption of Erythropoiesis

Motivated by the sensitivity analysis (Fig. 4.11) and by evidence that erythroblastic islands preferentially promote differentiation over proliferation, we tested whether selectively enhancing early erythroid production could mitigate AML-induced disruption. In a counterfactual simulation, we increased the basophilic erythroblast production rate ρ_{BasoE} while holding all AML-related parameters constant, and tracked erythropoietic outputs and AML burden over time from the calibrated baseline.

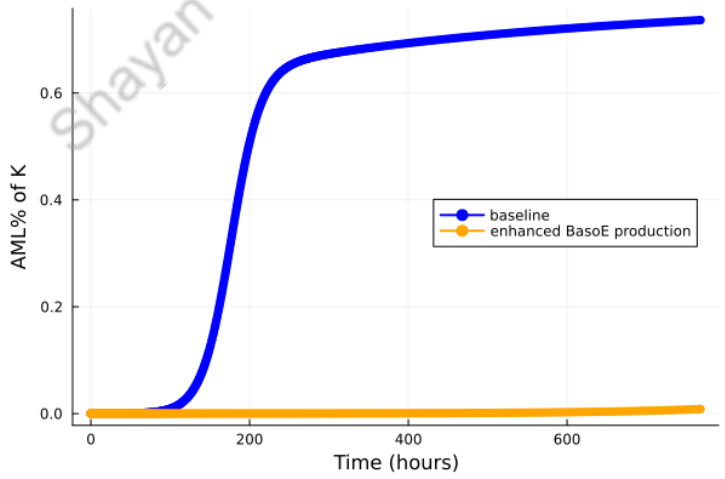

Figure 4.17: Model prediction for AML burden under baseline parameters (blue) versus enhanced basophilic-erythroblast production (orange). Under baseline conditions, AML expands sigmoidally after ∼150 hours and approaches ∼70% of carrying capacity (K) by 700 hours. By contrast, when ρ_{BasoE} is increased, AML growth remains near zero across the full 700-hour simulation.

Increasing ρ_{BasoE} produced a marked change in AML dynamics. Under baseline conditions,

AML exhibits sigmoidal growth, with rapid expansion after ∼150 h and reaching ∼70% of carrying capacity by 700 h. In contrast, elevating ρ_{BasoE} strongly suppressed AML expansion within the simulated time window.

This pattern is consistent with niche-mediated competition and with the models inferred bias towards EBI-driven differentiation support over proliferation support (typically $\beta_\gamma \gg \beta_\rho$). Enhancing erythroid throughput around the BasoE/PolyE transition increases occupancy of limiting niche resources and supportive signalling, thereby reducing effective capacity for leukaemic expansion. Notably, the suppression arises from altered resource allocation within the marrow microenvironment rather than a direct cytotoxic effect on AML cells.

Overall, these simulations suggest that selectively boosting erythroid progenitor production at the BasoE stage may mitigate AML-associated erythropoietic suppression. This is consistent with the sensitivity analysis identifying ρ_{BasoE} as an influential parameter, and it supports niche-targeted strategies that stabilise erythroid output under leukaemic stress.

From a translational perspective, this could be explored via interventions that preferentially enhance early erythroid production or maturation (e.g., cytokine modulation or pharmacological stimulation of progenitors). Experimental work is required to determine whether the same competitive regime can be achieved *in vivo* and whether similar protection arises from modulating other sensitive parameters identified in this study.

Discussion

5.1 Biological and Clinical Implications

Our results highlight erythroblastic islands (EBIs) as central organisers of erythropoietic regulation[10]. In AML, we observed progressive loss of nurse macrophages together with altered adhesion-marker phenotypes, including reduced CD169 and increased VCAM-1 surface levels. These changes are likely to weaken macrophage–erythroblast coupling that supports efficient erythroid maturation, including proliferative expansion, differentiation progression, and enucleation[10,126]. Consistent with this interpretation, perturbing macrophage-dependent niche support reduces erythroid output, including during stress erythropoiesis[101]. Together, these findings suggest that AML-associated erythropoietic failure reflects both structural EBI disruption and impaired adhesion-dependent signalling.

The progressive loss of $CD169^{+}$ nurse macrophages and EBI disorganisation aligns with anaemia and marrow-failure phenotypes reported in AML and supports a niche-disruption mechanism beyond marrow space competition alone[12,59,108]. More broadly, these data reinforce the concept that bone marrow macrophages are active regulators of erythropoiesis and that their dysfunction has substantial downstream consequences for erythroid output[10,41,101].

5.2 Therapeutic Implications of M-CSF Modulation

M-CSF (CSF-1) is a core niche-maintenance signal for macrophages and regulates macrophage survival and turnover through CSF1R signalling[46,98]. In AML, inflammatory and niche-remodelling mechanisms can disrupt macrophage-dependent support of erythropoiesis[6,12,59,108]. Within this framework, our results support a model in which impaired local support contributes to nurse macrophage loss and downstream erythropoietic dysfunction, consistent with the predicted coupling between nurse-cell decline and EBI collapse (Results; Fig. 4.13).

Consistent with this interpretation, exogenous M-CSF administration in leukaemic mice increased nurse macrophage abundance and partially improved erythropoiesis, with the strongest effects in early and intermediate erythroid compartments (I–III), while producing no measurable reduction in AML infiltration over the experimental window (data not shown). This reinforces M-CSF as a niche-stabilising intervention rather than a cytotoxic anti-leukaemic agent. Together with evidence linking M-CSF signalling to macrophage homeostasis[98,146] and context-dependent effects of M-CSF isoforms in MLL-AF9 AML[143], these results motivate further evaluation of M-CSF modulation as a supportive strategy to mitigate AML-associated anaemia.

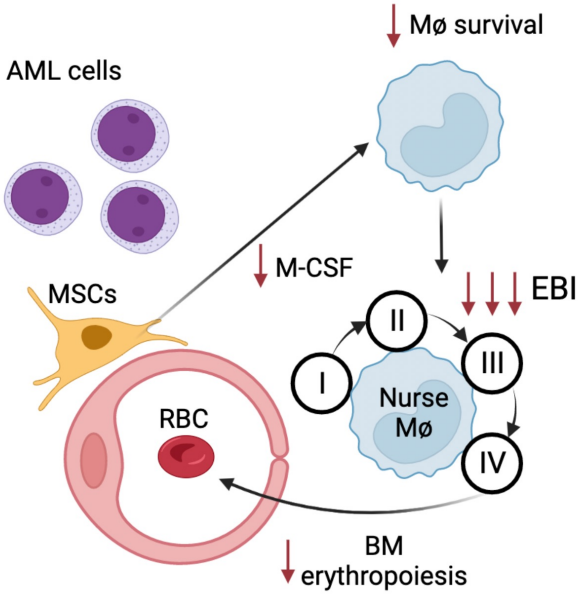

Figure 5.1: Schematic summary of the proposed mechanism. AML cells remodel the bone marrow microenvironment, leading to decreased *Csf1* expression by MSCs. Reduced M-CSF impairs nurse macrophage survival, resulting in collapse of erythroblastic islands (EBIs) and loss of bone marrow erythropoiesis. Exogenous M-CSF supplementation can partially rescue nurse-cell survival and restore erythropoietic function. This visual summary integrates experimental, transcriptomic, and modelling findings into a unifying framework[20,46,98].

5.3 Model Refinement and Integration

Our mathematical model integrates murine AML observations with mechanistic simulations of erythroid dynamics, reproducing depletion of late erythroid populations in leukaemic bone marrow and identifying nurse-cell turnover and niche-support signals as dominant regulators of erythropoietic efficiency[6,12,59,108]. Several refinements could strengthen the framework. First, parameter estimation would benefit from broader datasets, including single-cell transcriptomic profiling of EBI macrophages, to better constrain macrophage state heterogeneity and context-dependent responses. Second, extending the model to include coupled contributions of marrow and splenic erythropoiesis would improve physiological realism under stress and leukaemic conditions[39].

5.4 Model Strengths and Limitations

While the model provides an integrative platform linking experimental and computational findings, several limitations should be acknowledged. First, species-specific differences remain an important caveat: in our patient-derived samples, nurse macrophages did not show the same shifts in CD169 or VCAM-1 surface expression observed in the murine AML model. This discrepancy may reflect true divergence between human and mouse erythroid niches, but may also arise from technical constraints because intact EBIs can be fragile and difficult to preserve and isolate from clinical material[10,41].

Second, the model simplifies key regulatory layers of haematopoiesis. Erythropoietin-

driven feedback is represented implicitly rather than through an explicit endocrine loop, iron-handling regulation is not modelled explicitly[31,123,184], and stromal and vascular niche heterogeneity is lumped into effective parameters despite multiple niche cell types providing distinct regulatory signals in vivo[49,185]. Despite these simplifications, coupling experimental observations with mechanistic modelling enables hypothesis generation and prioritisation of experimentally tractable regulatory axes, providing a foundation for testing niche-stabilising therapeutic strategies.

Conclusion

Overview

This thesis investigated erythropoietic failure in acute myeloid leukaemia (AML) by integrating experimental measurements with mechanistic modelling. Across approaches, the results support a niche-driven mechanism in which disruption of erythroblastic islands (EBIs) and their central nurse macrophages contributes substantially to impaired red blood cell production.

Summary of the Study

Using murine MLL-AF9 AML models and human xenograft systems, we analysed how leukaemic remodelling of the bone marrow microenvironment alters erythropoiesis. A mechanistic ODE-based framework, calibrated to experimental fold-change data and interrogated with sensitivity analyses, was developed to quantify how macrophage support and cytokine availability shape erythroid output across increasing disease burden.

Key Findings

First, increasing leukaemic infiltration was associated with progressive loss of $CD169^{+}$ nurse macrophages and collapse of EBIs, coinciding with impaired terminal erythroid maturation and anaemia. Second, the calibrated model reproduced these erythroid dynamics under baseline and leukaemic conditions and captured how reduced macrophage support and altered cytokine availability suppress erythropoietic output. Third, global sensitivity analyses consistently prioritised the nurse-cell/M-CSF axis, together with additional macrophage- and erythroid-regulatory parameters, as dominant determinants of erythropoietic efficiency. Finally, exogenous M-CSF supplementation in leukaemic mice increased nurse macrophage abundance and partially improved erythropoiesis, supporting a niche-stabilisation mechanism and motivating further evaluation of macrophage-supportive interventions for AML-associated anaemia.

Scientific Contributions

This work provides an integrated experimental–computational framework that links AML-driven niche remodelling to erythropoietic failure. By combining quantitative data with a system-level model, it connects M-CSF–dependent macrophage survival, EBI integrity, and erythroid differentiation dynamics within a unified mechanistic structure. Collectively, these results clarify contributors to AML-associated anaemia and identify macrophage-supportive pathways as tractable targets for improving erythroid output under leukaemic stress.

Limitations

Important limitations remain. Species-specific differences constrain direct translation: in patient-derived material, nurse macrophages did not show the same CD169 or VCAM-1 shifts observed in murine AML, which may reflect biological divergence and/or the technical difficulty of recovering intact EBIs from clinical samples. The model also simplifies key

regulatory layers of haematopoiesis, omitting explicit erythropoietin (EPO) dynamics, clonal heterogeneity, and spatial microenvironmental constraints. In addition, although parameterisation was guided by available data and the literature, limited experimental coverage may reduce the quantitative precision of some estimates.

Future Directions

Future work should refine both the biological and computational components of this framework. Biologically, resolving heterogeneity among EBI macrophages using single-cell and multi-omics approaches will be important for determining whether specific nurse-macrophage subsets are preferentially disrupted in AML, and for clarifying the roles of transcriptional regulators such as KLF1 and GATA1 in macrophage–erythroblast communication. Computationally, extending the model to incorporate explicit EPO feedback, systemic iron regulation (including the hepcidin–ferroportin axis), and broader inflammatory cytokine networks would improve physiological realism and strengthen mechanistic inference. Translationally, validating model predictions in patient-derived AML systems and evaluating interventions targeting M-CSF and related niche-support pathways are essential next steps.

Final Remarks

Overall, this thesis supports a model in which AML-driven disruption of nurse macrophages and EBIs contributes substantially to erythropoietic failure. The integrated experimental and modelling framework established here provides a quantitative foundation for developing niche-stabilising strategies to improve red blood cell production and mitigate AML-associated anaemia.

Code and Software Availability

All computational code developed and used in this thesis is either publicly available or will be released following acceptance of the associated manuscript(s).

The Julia package implementing variogram-based global sensitivity analysis (VARS, GVARS, DVARS), `VariogramAnalysis.jl`, is available at:
https://github.com/Msturroc/VariogramAnalysis.jl

Additional scripts for comparative sensitivity analysis and benchmarking (Sobol, eFAST, PCE, VARS) are available at:
https://github.com/shayanjl/VARS-GSA

The code implementing the erythropoiesis model, including calibration routines, OAT analysis, and global sensitivity workflows, is currently maintained in a private repository linked to an unpublished manuscript. It will be made publicly available after the acceptance of the manuscript. Until then, access can be provided upon request to the author or supervising investigator.

Bibliography

[1] Shai Shimony, Maximilian Stahl, and Richard M Stone. "Acute Myeloid Leukemia: 2025 Update on Diagnosis, Risk-Stratification, and Management". In: *American Journal of Hematology* 100.5 (2025), pp. 860–891.

[2] Siok-Keen Tey and Steven W Lane. "Better the cure you know: why patients with AML 60 years of age should be offered early allogeneic stem cell transplantation". In: *Blood Advances* 6.5 (2022), pp. 1619–1622.

[3] Jodi J Lipof et al. "Allogeneic hematopoietic cell transplantation for older adults with acute myeloid leukemia". In: *Cancers* 10.6 (2018), p. 179.

[4] Celalettin Ustun et al. "Allogeneic hematopoietic cell transplantation compared to chemotherapy consolidation in older acute myeloid leukemia (AML) patients 60–75 years in first complete remission (CR1): an alliance (A151509), SWOG, ECOG-ACRIN, and CIBMTR study". In: *Leukemia* 33.11 (2019), pp. 2599–2609.

[5] Olgu Erkin Çnar et al. "Anemia in the patients with acute myeloid leukemia revisited: Prognostic importance of anemia on treatment-na¨ve patients". In: *Acta Medica* 56.2 (2025), pp. 116–121.

[6] Tian Y. Zhang et al. "IL-6 blockade reverses bone marrow failure induced by human acute myeloid leukemia". In: *Science Translational Medicine* 12.538 (2020), eaax5104. DOI: 10.1126/scitranslmed.aax5104.

[7] Amog P Urs, Chinmayee Goda, and Rohan Kulkarni. "Remodeling of the bone marrow microenvironment during acute myeloid leukemia progression". In: *Annals of Translational Medicine* 12.4 (2024), p. 63.

[8] Lena Behrmann, Jasmin Wellbrock, and Walter Fiedler. "Acute myeloid leukemia and the bone marrow nichetake a closer look". In: *Frontiers in oncology* 8 (2018), p. 444.

[9] Antoniana Batsivari, William Grey, and Dominique Bonnet. "Understanding of the crosstalk between normal residual hematopoietic stem cells and the leukemic niche in acute myeloid leukemia". In: *Experimental hematology* 95 (2021), pp. 23–30.

[10] Joel A. Chasis and Narla Mohandas. "Erythroblastic islands: niches for erythropoiesis". In: *Blood* 112.3 (2008), pp. 470–478. DOI: 10.1182/blood-2008-03-077883.

[11] Andrew Chow et al. "CD169+ macrophages provide a niche promoting erythropoiesis under homeostasis and stress". In: *Nature medicine* 19.4 (2013), pp. 429–436.

[12] Delfim Duarte et al. "Inhibition of endosteal vascular niche remodeling rescues hematopoietic stem cell loss in AML". In: *Cell stem cell* 22.1 (2018), pp. 64–77.

[13] Maria Krevvata et al. "Inhibition of leukemia cell engraftment and disease progression in mice by osteoblasts". In: *Blood, The Journal of the American Society of Hematology* 124.18 (2014), pp. 2834–2846.

[14] Débora Bifano Pimenta et al. "The bone marrow microenvironment mechanisms in acute myeloid leukemia". In: *Frontiers in Cell and Developmental Biology* 9 (2021), p. 764698.

[15] Katerina E Miari et al. "Macrophages in acute myeloid leukaemia: Significant players in therapy resistance and patient outcomes". In: *Frontiers in cell and developmental biology* 9 (2021), p. 692800.

[16] Zi-Jun Xu et al. "The M2 macrophage marker CD206: a novel prognostic indicator for acute myeloid leukemia". In: *Oncoimmunology* 9.1 (2020), p. 1683347.

[17] Haifa A Al-Matari et al. “Soluble CD206 and CD163 as novel prognostic biomarkers in adult acute myeloid leukemia”. In: *The Journal of Basic and Applied Zoology* 85.1 (2024), p. 52.

[18] Jean-Pierre Lévesque et al. “Macrophages form erythropoietic niches and regulate iron homeostasis to adapt erythropoiesis in response to infections and inflammation”. In: *Experimental Hematology* 103 (2021), pp. 1–14.

[19] Jian Bai et al. “CD169-CD43 interaction is involved in erythroblastic island formation and erythroid differentiation”. In: *Haematologica* 108.8 (2023), p. 2205.

[20] Qiaozhi Wei et al. “Maea expressed by macrophages, but not erythroblasts, maintains postnatal murine bone marrow erythroblastic islands”. In: *Blood* 133.11 (2019), pp. 1222–1232. DOI: 10.1182/blood-2018-11-888180.

[21] Marta Lopes et al. “Loss of erythroblasts in acute myeloid leukemia causes iron redistribution with clinical implications”. In: *Blood Advances* 5.16 (2021), pp. 3102–3112. DOI: 10.1182/bloodadvances.2021004373.

[22] Deepa Manwani and James J Bieker. “The erythroblastic island”. In: *Current topics in developmental biology* 82 (2008), pp. 23–53.

[23] Alisha May and Lesley M Forrester. “The erythroblastic island niche: modeling in health, stress, and disease”. In: *Experimental Hematology* 91 (2020), pp. 10–21.

[24] Sarah Weber et al. “The clinical significance of iron overload and iron metabolism in myelodysplastic syndrome and acute myeloid leukemia”. In: *Frontiers in immunology* 11 (2021), p. 627662.

[25] Aaron D Goldberg and Martin S Tallman. “Down for the count in acute myeloid leukemia”. In: *Blood, The Journal of the American Society of Hematology* 128.18 (2016), pp. 2195–2197.

[26] Marco G Cecchini et al. “Role of colony stimulating factor-1 in the establishment and regulation of tissue macrophages during postnatal development of the mouse”. In: *Development* 120.6 (1994), pp. 1357–1372.

[27] Simranpreet Kaur et al. “Stable colony-stimulating factor 1 fusion protein treatment increases hematopoietic stem cell pool and enhances their mobilisation in mice”. In: *Journal of Hematology & Oncology* 14.1 (2021), p. 3.

[28] Kathryn A Skelding et al. “Bone marrow microenvironment as a source of new drug targets for the treatment of acute myeloid leukaemia”. In: *International Journal of Molecular Sciences* 24.1 (2022), p. 563.

[29] Andrea Zivot et al. “Erythropoiesis: insights into pathophysiology and treatments in 2017”. In: *Molecular Medicine* 24.1 (2018), p. 11.

[30] Arthur C. Guyton and John E. Hall. *Textbook of Medical Physiology*. 11th ed. Philadelphia: Elsevier Saunders, 2006. ISBN: 9780721602400.

[31] Mark J. Koury and Prem Ponka. “New insights into erythropoiesis: the roles of folate, vitamin B12, and iron”. In: *Annual Review of Nutrition* 24 (2004), pp. 105–131. DOI: 10.1146/annurev.nutr.24.012003.132306.

[32] Anwesha Chaudhury et al. “Single-cell modeling of routine clinical blood tests reveals transient dynamics of human response to blood loss”. In: *Elife* 8 (2019), e48590.

[33] Chong Yang and Toshio Suda. “Microenvironmental dynamics in steady-state and stress erythropoiesis”. In: *Blood Science* 7.01 (2025), pp. 1–8.

[34] Bo O Zhou et al. “Leptin-receptor-expressing mesenchymal stromal cells represent the main source of bone formed by adult bone marrow”. In: *Cell stem cell* 15.2 (2014), pp. 154–168.

[35] Stefano Comazzetto et al. “Restricted hematopoietic progenitors and erythropoiesis require SCF from leptin receptor+ niche cells in the bone marrow”. In: *Cell stem cell* 24.3 (2019), pp. 477–486.
[36] Robert F Paulson et al. “Stress erythropoiesis is a key inflammatory response”. In: *Cells* 9.3 (2020), p. 634.
[37] Malay Haldar. “Stressed about erythropoiesis: EBI macrophages”. In: *Blood, The Journal of the American Society of Hematology* 132.24 (2018), pp. 2530–2532.
[38] Laura F Bennett et al. “Inflammation induces stress erythropoiesis through heme-dependent activation of SPI-C”. In: *Science signaling* 12.598 (2019), eaap7336.
[39] K Pantel et al. “A mathematical model of erythropoiesis in mice and rats. Part 4: Differences between bone marrow and spleen”. In: *Cell Proliferation* 23.4 (1990), pp. 283–297.
[40] Jiina Holá et al. “Regeneration of Murine Erythropoiesis in Individual Bone Marrow Regions (Bones) and Spleen in Lethally Irradiated Marrow Graft Recipients”. In: *Acta Veterinaria Brno* 54.1-2 (1985), pp. 53–59.
[41] Wei Li et al. “Erythroblastic island macrophages shape normal erythropoiesis and drive associated disorders in erythroid hematopoietic diseases”. In: *Frontiers in Cell and Developmental Biology* 8 (2021), p. 613885.
[42] Thomas RL Klei et al. “From the cradle to the grave: the role of macrophages in erythropoiesis and erythrophagocytosis”. In: *Frontiers in immunology* 8 (2017), p. 73.
[43] Paraskevi Rea Oikonomidou and Stefano Rivella. “What can we learn from ineffective erythropoiesis in thalassemia?” In: *Blood Reviews* 32.2 (2018), pp. 130–143. DOI: 10.1016/j.blre.2017.10.002.
[44] Pedro Ramos et al. “Macrophages support pathological erythropoiesis in polycythemia vera and β-thalassemia”. In: *Nature Medicine* 19.4 (2013), pp. 437–445. DOI: 10.1038/nm.3126.
[45] Stephan Fischer et al. “Modeling erythroblastic islands: using a hybrid model to assess the function of central macrophage”. In: *Journal of theoretical biology* 298 (2012), pp. 92–106.
[46] John A Hamilton. “Colony-stimulating factors in inflammation and autoimmunity”. In: *Nature Reviews Immunology* 8.7 (2008), pp. 533–544.
[47] Anuj Sehgal, Katharine M. Irvine, and David A. Hume. “Functions of macrophage colony-stimulating factor (CSF1) in development, homeostasis, and tissue repair”. In: *Seminars in Immunology* 54 (2021), p. 101509. DOI: 10.1016/j.smim.2021.101509.
[48] Manar S. Shafat et al. “The bone marrow microenvironment–Home of the leukemic blasts”. In: *Blood Reviews* 31.5 (2017), pp. 277–286. DOI: 10.1016/j.blre.2017.03.004.
[49] Sean J. Morrison and David T. Scadden. “The bone marrow niche for haematopoietic stem cells”. In: *Nature* 505.7483 (2014), pp. 327–334. DOI: 10.1038/nature12984.
[50] Avital Mendelson and Paul S. Frenette. “Hematopoietic stem cell niche maintenance during homeostasis and regeneration”. In: *Nature Medicine* 20.8 (2014), pp. 833–846. DOI: 10.1038/nm.3647.
[51] Binod Kumar et al. “Acute myeloid leukemia transforms the bone marrow niche into a leukemia-permissive microenvironment through exosome secretion”. In: *Leukemia* 32.3 (2018), pp. 575–587. DOI: 10.1038/leu.2017.259.

[52] Francis Mussai et al. “Acute myeloid leukemia creates an arginase-dependent immunosuppressive microenvironment”. In: *Blood* 122.5 (2013), pp. 749–758. DOI: 10.1182/blood-2013-01-480129.

[53] Peter van Galen et al. “Single-cell RNA-seq reveals AML hierarchies relevant to disease progression and immunity”. In: *Cell* 176.6 (2019), pp. 1265–1281. DOI: 10.1016/j.cell.2019.01.031.

[54] Isabel Weinhäuser et al. “M2 macrophages drive leukemic transformation by imposing resistance to phagocytosis and improving mitochondrial metabolism”. In: *Science Advances* 9.15 (2023), eadf8522. DOI: 10.1126/sciadv.adf8522.

[55] Ruxanda Moschoi et al. “Protective mitochondrial transfer from bone marrow stromal cells to acute myeloid leukemic cells during chemotherapy”. In: *Blood* 128.2 (2016), pp. 253–264. DOI: 10.1182/blood-2016-02-700146.

[56] Amina M. Abdul-Aziz et al. “Acute myeloid leukemia induces protumoral p16^{INK4a}-driven senescence in the bone marrow microenvironment”. In: *Blood* 133.5 (2019), pp. 446–456. DOI: 10.1182/blood-2018-09-876136.

[57] Norman E. Sharpless and Charles J. Sherr. “Forging a signature of in vivo senescence”. In: *Nature Reviews Cancer* 15.7 (2015), pp. 397–408. DOI: 10.1038/nrc3973.

[58] Judith Campisi. “Aging, cellular senescence, and cancer”. In: *Annual Review of Physiology* 75 (2013), pp. 685–705. DOI: 10.1146/annurev-physiol-030212-183653.

[59] Maher Hanoun et al. “Acute myelogenous leukemia-induced sympathetic neuropathy promotes malignancy in an altered hematopoietic stem cell niche”. In: *Cell stem cell* 15.3 (2014), pp. 365–375.

[60] Adam J Mead et al. “Niche-mediated depletion of the normal hematopoietic stem cell reservoir by Flt3-ITD–induced myeloproliferation”. In: *Journal of Experimental Medicine* 214.7 (2017), pp. 2005–2021.

[61] Geoffrey L. Uy et al. “A phase 1/2 study of chemosensitization with the CXCR4 antagonist plerixafor in relapsed or refractory acute myeloid leukemia”. In: *Blood* 119.17 (2012), pp. 3917–3924. DOI: 10.1182/blood-2011-10-383406.

[62] Byung-Sik Cho, Hee-Je Kim, and Marina Konopleva. “Targeting the CXCL12/CXCR4 axis in acute myeloid leukemia: from bench to bedside”. In: *The Korean Journal of Internal Medicine* 32.2 (2017), pp. 248–257. DOI: 10.3904/kjim.2016.253.

[63] Allison L. Boyd et al. “Acute myeloid leukaemia disrupts endogenous myelo-erythropoiesis by compromising the adipocyte bone marrow niche”. In: *Nature Cell Biology* 19.11 (2017), pp. 1336–1347. DOI: 10.1038/ncb3625.

[64] Lindsay Wilde and Margaret Kasner. “Targeting CD47: many misses; hopeful for a hit”. In: *Blood* 145.5 (2025), pp. 460–462. DOI: 10.1182/blood.2024022361.

[65] Andrea Marra et al. “CD47 expression in acute myeloid leukemia varies according to genotype”. In: *Haematologica* 108.12 (2023), pp. 3491–3503. DOI: 10.3324/haematol.2023.282993.

[66] Salvador Chulián et al. “Mathematical models of leukaemia and its treatment: a review”. In: *SeMA Journal* 79.3 (2022), pp. 441–486. DOI: 10.1007/s40324-022-00296-z.

[67] L. G. Lajtha and R. Oliver. “Studies on the Kinetics of Erythropoiesis: A Model of the Erythron”. In: *Haemopoiesis*. Ed. by G. Wolstenholme. Churchill, 1960, pp. 289–314.

[68] H. E. Wichmann et al. "A Mathematical Model of Erythropoiesis in Man". In: *Mathematical Models in Medicine: Workshop, Mainz, March 1976*. Springer, 1976, pp. 159–179.
[69] M Loeffler et al. "A mathematical model of erythropoiesis in mice and rats Part 1: Structure of the model". In: *Cell Proliferation* 22.1 (1989), pp. 13–30.
[70] HE Wichmann et al. "A mathematical model of erythropoiesis in mice and rats Part 2: Stimulated erythropoiesis". In: *Cell Proliferation* 22.1 (1989), pp. 31–49.
[71] H Wulff et al. "A mathematical model of erythropoiesis in mice and rats Part 3: Suppressed erythropoiesis". In: *Cell Proliferation* 22.1 (1989), pp. 51–61.
[72] Ingo Roeder and Markus Loeffler. "A novel dynamic model of hematopoietic stem cell organization based on the concept of within-tissue plasticity". In: *Experimental hematology* 30.8 (2002), pp. 853–861.
[73] Franziska Michor et al. "Dynamics of chronic myeloid leukaemia". In: *Nature* 435.7046 (2005), pp. 1267–1270.
[74] Ingo Roeder et al. "Dynamic modeling of imatinib-treated chronic myeloid leukemia: functional insights and clinical implications". In: *Nature medicine* 12.10 (2006), pp. 1181–1184.
[75] Thomas Stiehl and Anna Marciniak-Czochra. "Mathematical Modeling of Leukemogenesis and Cancer Stem CellDynamics". In: *Mathematical Modelling of Natural Phenomena* 7.1 (2012), pp. 166–202.
[76] Thomas Stiehl et al. "Clonal selection and therapy resistance in acute leukaemias: mathematical modelling explains different proliferation patterns at diagnosis and relapse". In: *Journal of The Royal Society Interface* 11.94 (2014), p. 20140079.
[77] Anna Marciniak-Czochra et al. "Modeling of asymmetric cell division in hematopoietic stem cells: regulation of self-renewal is essential for efficient repopulation". In: *Stem Cells and Development* 18.3 (2009), pp. 377–386.
[78] Ignacio A Rodriguez-Brenes, Natalia L Komarova, and Dominik Wodarz. "Evolutionary dynamics of feedback escape and the development of stem-cell–driven cancers". In: *Proceedings of the National Academy of Sciences* 108.47 (2011), pp. 18983–18988.
[79] Adam L MacLean, Cristina Lo Celso, and Michael PH Stumpf. "Population dynamics of normal and leukaemia stem cells in the haematopoietic stem cell niche show distinct regimes where leukaemia will be controlled". In: *Journal of the Royal Society Interface* 10.81 (2013), p. 20120968.
[80] Jianfeng Jiao, Min Luo, and Ruiqi Wang. "Feedback regulation in a stem cell model with acute myeloid leukaemia". In: *BMC Systems Biology* 12.Suppl 4 (2018), p. 43.
[81] Helena L Crowell, Adam L MacLean, and Michael PH Stumpf. "Feedback mechanisms control coexistence in a stem cell model of acute myeloid leukaemia". In: *Journal of Theoretical Biology* 401 (2016), p. 43.
[82] Helene Hoffmann et al. "How to predict relapse in leukemia using time series data: A comparative in silico study". In: *PLOS ONE* 16.11 (2021), e0256585. DOI: 10.1371/journal.pone.0256585.
[83] Khanh N. Dinh et al. "Predicting time to relapse in acute myeloid leukemia through stochastic modeling of minimal residual disease based on clonality data". In: *Computational and Systems Oncology* 1.3 (2021), e1026. DOI: 10.1002/cso2.1026.
[84] Laleh Haghverdi and Leif S. Ludwig. "Single-cell multi-omics and lineage tracing to dissect cell fate decision-making". In: *Stem Cell Reports* 18.1 (2023), pp. 13–25. DOI: 10.1016/j.stemcr.2022.11.006.

[85] Léonard Hérault et al. “Single-cell RNA-seq reveals a concomitant delay in differentiation and cell cycle of aged hematopoietic stem cells”. In: *BMC Biology* 19.1 (2021), p. 19. DOI: 10.1186/s12915-021-00955-z.

[86] Lennart Kester and Alexander van Oudenaarden. “Single-cell transcriptomics meets lineage tracing”. In: *Cell Stem Cell* 23.2 (2018), pp. 166–179. DOI: 10.1016/j.stem.2018.04.003.

[87] Ingmar Glauche and Carsten Marr. “Mechanistic models of blood cell fate decisions in the era of single-cell data”. In: *Current Opinion in Systems Biology* 28 (2021), p. 100355. DOI: 10.1016/j.coisb.2021.100355.

[88] Weijie Cao et al. “GM-CSF impairs erythropoiesis by disrupting erythroblastic island formation via macrophages”. In: *Journal of Translational Medicine* 20.1 (2022), p. 11. DOI: 10.1186/s12967-021-03214-5.

[89] Matthias Wunderlich et al. “AML xenograft efficiency is significantly improved in NOD/SCID-IL2RG mice constitutively expressing human SCF, GM-CSF and IL-3”. In: *Leukemia* 24.10 (2010), pp. 1785–1788. DOI: 10.1038/leu.2010.158.

[90] François E. Nicolini et al. “NOD/SCID mice engineered to express human IL-3, GM-CSF and Steel factor constitutively mobilize engrafted human progenitors and compromise human stem cell regeneration”. In: *Leukemia* 18.2 (2004), pp. 341–347. DOI: 10.1038/sj.leu.2403247.

[91] European Parliament and Council of the European Union. *Directive 2010/63/EU of the European Parliament and of the Council of 22 September 2010 on the protection of animals used for scientific purposes*. https://eur-lex.europa.eu/legal-content/EN/TXT/PDF/?uri=CELEX:32010L0063. Official Journal of the European Union, L 276, pp. 33–79. 2010.

[92] Xinyue Chen et al. “MLL-AF9 initiates transformation from fast-proliferating myeloid progenitors”. In: *Nature Communications* 10.1 (2019), p. 5767. DOI: 10.1038/s41467-019-13648-5.

[93] Marta Galán-Díez et al. “Subversion of serotonin receptor signaling in osteoblasts by kynurenine drives acute myeloid leukemia”. In: *Cancer Discovery* 12.4 (2022), pp. 1106–1127. DOI: 10.1158/2159-8290.CD-21-0936.

[94] Syed A. Mian, Fernando Anjos-Afonso, and Dominique Bonnet. “Advances in human immune system mouse models for studying human hematopoiesis and cancer immunotherapy”. In: *Frontiers in Immunology* 11 (2021), p. 619236. DOI: 10.3389/fimmu.2020.619236.

[95] Katie Giger Seu et al. “Unraveling macrophage heterogeneity in erythroblastic islands”. In: *Frontiers in Immunology* 8 (2017), p. 1140. DOI: 10.3389/fimmu.2017.01140.

[96] Joshua Tay et al. “Imaging flow cytometry reveals that granulocyte colony-stimulating factor treatment causes loss of erythroblastic islands in the mouse bone marrow”. In: *Experimental Hematology* 82 (2020), pp. 33–42. DOI: 10.1016/j.exphem.2019.11.003.

[97] Laurel Romano et al. “Erythroblastic islands foster granulopoiesis in parallel to terminal erythropoiesis”. In: *Blood* 140.14 (2022), pp. 1621–1634. DOI: 10.1182/blood.2021013640.

[98] E. Richard Stanley and Violeta Chitu. “CSF-1 receptor signaling in myeloid cells”. In: *Cold Spring Harbor Perspectives in Biology* 6.6 (2014), a021857. DOI: 10.1101/cshperspect.a021857.

[99] Eiji Asakura et al. “Intravenously administered macrophage colony-stimulating factor (M-CSF) specifically acts on the spleen, resulting in the increasing and activating spleen macrophages for cytokine production in mice”. In: *Immunopharmacology* 37.1 (1997), pp. 7–14. DOI: 10.1016/S0162-3109(97)00027-6.

[100] Fabien Crauste et al. “Adding self-renewal in committed erythroid progenitors improves the biological relevance of a mathematical model of erythropoiesis”. In: *Journal of Theoretical Biology* 250.2 (2008), pp. 322–338. DOI: 10.1016/j.jtbi.2007.09.041.

[101] Tatiana Ulyanova, Susan R. Phelps, and Thalia Papayannopoulou. “The macrophage contribution to stress erythropoiesis: when less is enough”. In: *Blood* 128.13 (2016), pp. 1756–1765. DOI: 10.1182/blood-2016-06-722827.

[102] Omar S. Hajjawi. “Human red blood cells-1”. In: *American Journal of Life Sciences* 1.5 (2013), pp. 195–214. DOI: 10.11648/j.ajls.20130105.13.

[103] Nidal H. Al-Huniti et al. “Pharmacodynamic analysis of changes in reticulocyte subtype distribution in phlebotomy-induced stress erythropoiesis”. In: *Journal of Pharmacokinetics and Pharmacodynamics* 32.3 (2005), pp. 359–376. DOI: 10.1007/s10928-005-3052-3.

[104] Allison Mayle et al. “Mouse hematopoietic stem cell identification and analysis”. In: *Cytometry Part A* 83.1 (2012), p. 27. DOI: 10.1002/cyto.a.22029.

[105] Charles-Etienne Lebert-Ghali et al. “HoxA cluster is haploinsufficient for activity of hematopoietic stem and progenitor cells”. In: *Experimental Hematology* 38.11 (2010), pp. 1074–1086. DOI: 10.1016/j.exphem.2010.07.004.

[106] Adam L. MacLean, Sarah Filippi, and Michael P. H. Stumpf. “The ecology in the hematopoietic stem cell niche determines the clinical outcome in chronic myeloid leukemia”. In: *Proceedings of the National Academy of Sciences of the United States of America* 111.10 (2014), pp. 3883–3888. DOI: 10.1073/pnas.1317072111.

[107] Chenxu Zhu and Thomas Stiehl. “Modelling post-chemotherapy stem cell dynamics in the bone marrow niche of AML patients”. In: *Scientific Reports* 14.1 (2024), p. 25060. DOI: 10.1038/s41598-024-75429-7.

[108] Farideh Miraki-Moud et al. “Acute myeloid leukemia does not deplete normal hematopoietic stem cells but induces cytopenias by impeding their differentiation”. In: *Proceedings of the National Academy of Sciences* 110.33 (2013), pp. 13576–13581.

[109] Makio Ogawa. “Differentiation and proliferation of hematopoietic stem cells”. In: (1993).

[110] Matthieu Duchmann, Lucie Laplane, and Raphael Itzykson. “Clonal architecture and evolutionary dynamics in acute myeloid leukemias”. In: *Cancers* 13.19 (2021), p. 4887.

[111] Hui Cheng et al. “Leukemic marrow infiltration reveals a novel role for Egr3 as a potent inhibitor of normal hematopoietic stem cell proliferation”. In: *Blood, The Journal of the American Society of Hematology* 126.11 (2015), pp. 1302–1313.

[112] MJ Cline and DW Golde. “Cellular interactions in haematopoiesis”. In: *Nature* 277.5693 (1979), pp. 177–181.

[113] Sara Gardenghi et al. “Distinct roles for hepcidin and interleukin-6 in the recovery from anemia in mice injected with heat-killed Brucella abortus”. In: *Blood* 123.8 (2014), pp. 1137–1145. DOI: 10.1182/blood-2013-09-527176.

[114] Bryan J. McCranor et al. “Investigation of the role of interleukin-6 and hepcidin antimicrobial peptide in the development of anemia with age”. In: *Haematologica* 98.10 (2013), pp. 1633–1640. DOI: 10.3324/haematol.2013.083105.

[115] Jacqueline M. Langdon et al. "Hepcidin-dependent and hepcidin-independent regulation of erythropoiesis in a mouse model of anemia of chronic inflammation". In: *American Journal of Hematology* 89.5 (2014), pp. 470–479. DOI: 10.1002/ajh.23670.

[116] Lisa Bast et al. "Computational modeling of stem and progenitor cell kinetics identifies plausible hematopoietic lineage hierarchies". In: *Iscience* 24.2 (2021).

[117] Joan Wright Goodman and L. H. Smith. "Erythrocyte life span in normal mice and in radiation bone marrow chimeras". In: *American Journal of Physiology* 200.4 (1961), pp. 764–770.

[118] Arvind Dev et al. "During EPO or anemia challenge, erythroid progenitor cells transit through a selectively expandable proerythroblast pool". In: *Blood* 116.24 (2010), pp. 5334–5346. DOI: 10.1182/blood-2010-05-285163.

[119] Jing Liu et al. "Quantitative analysis of murine terminal erythroid differentiation in vivo: novel method to study normal and disordered erythropoiesis". In: *Blood* 121.8 (2013), e43–e49. DOI: 10.1182/blood-2012-09-456079.

[120] Richard C. van der Wath et al. "Estimating dormant and active hematopoietic stem cell kinetics through extensive modeling of bromodeoxyuridine label-retaining cell dynamics". In: *PLoS ONE* 4.9 (2009), e6972. DOI: 10.1371/journal.pone.0006972.

[121] Anna S. Eisele et al. "Erythropoietin directly affects single hematopoietic stem cell differentiation after transplantation". In: *Haematologica* 105.12 (2020), e629–e633. DOI: 10.3324/haematol.2019.243626.

[122] Petr Páral et al. "Cell cycle and differentiation of Sca-1+ and Sca-1- hematopoietic stem and progenitor cells". In: *Cell Cycle* 17.16 (2018), pp. 1979–1991. DOI: 10.1080/15384101.2018.1515555.

[123] Shilpa M. Hattangadi et al. "From stem cell to red cell: regulation of erythropoiesis at multiple levels by multiple proteins, RNAs, and chromatin modifications". In: *Blood* 118.24 (2011), pp. 6258–6268. DOI: 10.1182/blood-2011-07-356006.

[124] P. Milenkovi, R. Ruvidi, and V. Pavlovi-Kentera. "Cell cycle time of erythroid cells in mice with normal and stimulated erythropoiesis". In: *Strahlentherapie* 153.11 (1977), pp. 780–785.

[125] Alexis L. Caulier and Vijay G. Sankaran. "Molecular and cellular mechanisms that regulate human erythropoiesis". In: *Blood* 139.16 (2022), pp. 2450–2459. DOI: 10.1182/blood.2021014127.

[126] Melissa M. Rhodes et al. "Adherence to macrophages in erythroblastic islands enhances erythroblast proliferation and increases erythrocyte production by a different mechanism than erythropoietin". In: *Blood* 111.3 (2008), pp. 1700–1708. DOI: 10.1182/blood-2007-07-102491.

[127] Karl Olof Skårberg. "Cellularity and cell proliferation rates in human bone marrow: I. An in vivo method to estimate the total marrow cellularity in man". In: *Acta Medica Scandinavica* 195.1–6 (1974), pp. 291–299.

[128] Samuel H. Cheshier et al. "In vivo proliferation and cell cycle kinetics of long-term self-renewing hematopoietic stem cells". In: *Proceedings of the National Academy of Sciences* 96.6 (1999), pp. 3120–3125. DOI: 10.1073/pnas.96.6.3120.

[129] Christa Muller-Sieburg and Hans B. Sieburg. "Stem cell aging: survival of the laziest?" In: *Cell Cycle* 7.24 (2008), pp. 3798–3804. DOI: 10.4161/cc.7.24.7313.

[130] Jos Domen, Samuel H. Cheshier, and Irving L. Weissman. "The role of apoptosis in the regulation of hematopoietic stem cells: Overexpression of Bcl-2 increases both

their number and repopulation potential". In: *Journal of Experimental Medicine* 191.2 (2000), pp. 253–264.

[131] Jaime Murphy et al. "The prolonged life-span of alveolar macrophages". In: *American Journal of Respiratory Cell and Molecular Biology* 38.4 (2008), pp. 380–385. DOI: 10.1165/rcmb.2007-0224OC.

[132] Kinga Krawiec et al. "Targeting apoptosis in AML: where do we stand?" In: *Cancers* 14.20 (2022), p. 4995. DOI: 10.3390/cancers14204995.

[133] Abhinav Diwan et al. "Unrestrained erythroblast development in Nix$^{-/-}$ mice reveals a mechanism for apoptotic modulation of erythropoiesis". In: *Proceedings of the National Academy of Sciences* 104.16 (2007), pp. 6794–6799.

[134] Emmanuelle Passegué et al. "Global analysis of proliferation and cell cycle gene expression in the regulation of hematopoietic stem and progenitor cell fates". In: *Journal of Experimental Medicine* 202.11 (2005), pp. 1599–1611.

[135] R. De Maria et al. "Apoptotic role of Fas/Fas ligand system in the regulation of erythropoiesis". In: *Blood* 93.3 (1999), pp. 796–803.

[136] Raymond Liang and Saghi Ghaffari. "Advances in understanding the mechanisms of erythropoiesis in homeostasis and disease". In: *British Journal of Haematology* 174.5 (2016), pp. 661–673. DOI: 10.1111/bjh.14134.

[137] Genève Perron-Deshaies et al. "Impact of erythropoietin production by erythroblastic island macrophages on homeostatic murine erythropoiesis". In: *International Journal of Molecular Sciences* 21.23 (2020), p. 8930. DOI: 10.3390/ijms21238930.

[138] Christopher Y. Kim et al. "Low-dose dietary fish oil improves RBC deformability without improving post-transfusion recovery in mice". In: *Nutrients* 15.20 (2023), p. 4456. DOI: 10.3390/nu15204456.

[139] Hitoshi Takizawa et al. "Dynamic variation in cycling of hematopoietic stem cells in steady state and inflammation". In: *Journal of Experimental Medicine* 208.2 (2011), pp. 273–284. DOI: 10.1084/jem.20101643.

[140] Katrin Busch et al. "Fundamental properties of unperturbed haematopoiesis from stem cells in vivo". In: *Nature* 518.7540 (2015), pp. 542–546. DOI: 10.1038/nature14242.

[141] Daniel Ward et al. "Mathematical modeling reveals differential effects of erythropoietin on proliferation and lineage commitment of human hematopoietic progenitors in early erythroid culture". In: *Haematologica* 101.3 (2016), pp. 286–296. DOI: 10.3324/haematol.2015.133728.

[142] S.-A. Killmann et al. "Mitotic indices of human bone marrow cells. III. Duration of some phases of erythrocytic and granulocytic proliferation computed from mitotic indices". In: *Blood* 24 (1964), pp. 267–280.

[143] Rong Wang et al. "Heterogeneous effects of M-CSF isoforms on the progression of MLL-AF 9 leukemia". In: *Immunology and Cell Biology* 96.2 (2018), pp. 190–203.

[144] Donald Metcalf. "The colony-stimulating factors and cancer". In: *Nature Reviews Cancer* 10.6 (2010), pp. 425–434.

[145] Makoto Akashi, Masaki Saito, and H. Phillip Koeffler. "Lymphotoxin: stimulation and regulation of colony-stimulating factors in fibroblasts". In: *Journal of Immunology* (1989), pp. 2383–2390.

[146] Daigo Hashimoto et al. "Pretransplant CSF-1 therapy expands recipient macrophages and ameliorates GVHD after allogeneic hematopoietic cell transplantation". In: *Journal of Experimental Medicine* 208.5 (2011), pp. 1069–1082. DOI: 10.1084/jem.20101709.

[147] Xu-Ming Dai et al. “Targeted disruption of the mouse colony-stimulating factor 1 receptor gene results in osteopetrosis, mononuclear phagocyte deficiency, increased primitive progenitor cell frequencies, and reproductive defects”. In: *Blood* 99.1 (2002), pp. 111–120. DOI: 10.1182/blood.V99.1.111.

[148] Martin G. Sanda et al. “Intravenous administration of recombinant human macrophage colony-stimulating factor to patients with metastatic cancer: a phase I study”. In: *Journal of Clinical Oncology* 10.10 (1992), pp. 1643–1649. DOI: 10.1200/JCO.1992.10.10.1643.

[149] Deborah J. Gow et al. “Characterisation of a Novel Fc Conjugate of Macrophage Colony-stimulating Factor”. In: *Molecular Therapy* 22.9 (2014), pp. 1580–1592. DOI: 10.1038/mt.2014.112.

[150] Christopher Rackauckas and Qing Nie. “Differentialequations. jl–a performant and feature-rich ecosystem for solving differential equations in julia”. In: *Journal of open research software* 5.1 (2017), pp. 15–15.

[151] Robert Feldt and contributors. *BlackBoxOptim.jl: Black-box optimization algorithms for Julia*. https://github.com/robertfeldt/BlackBoxOptim.jl. Accessed 2026-02-07. 2018.

[152] Daan Wierstra et al. “Natural evolution strategies”. In: *The Journal of Machine Learning Research* 15.1 (2014), pp. 949–980.

[153] SciML Development Team. *BlackBoxOptim.jl Optimization Package*. https://docs.sciml.ai/Optimization/stable/optimization_packages/blackboxoptim/. Accessed 2026-02-07. 2023.

[154] Vaibhav Kumar Dixit and Christopher Rackauckas. “GlobalSensitivity. jl: Performant and Parallel GlobalSensitivity Analysis with Julia”. In: *Journal of Open Source Software* 7.76 (2022).

[155] Cornelis J. Pronk et al. “Elucidation of the phenotypic, functional, and molecular topography of a myeloerythroid progenitor cell hierarchy”. In: *Cell Stem Cell* 1.4 (2007), pp. 428–442. DOI: 10.1016/j.stem.2007.10.005.

[156] Koichi Akashi et al. “Transcriptional accessibility for genes of multiple tissues and hematopoietic lineages is hierarchically controlled during early hematopoiesis”. In: *Blood* 101.2 (2003), pp. 383–389. DOI: 10.1182/blood-2002-06-1760.

[157] Joel Tellinghuisen. “Weighted least-squares in calibration: What difference does it make?” In: *Analyst* 132.6 (2007), pp. 536–543.

[158] Qiaoling Charlene Zeng et al. “Weighted least squares in calibration: estimating data variance functions in high-performance liquid chromatography”. In: *Journal of Chromatography A* 1206.2 (2008), pp. 147–152.

[159] Emanuele Borgonovo and Elmar Plischke. “Sensitivity analysis: A review of recent advances”. In: *European Journal of Operational Research* 248.3 (2016), pp. 869–887.

[160] Max D Morris. “Factorial sampling plans for preliminary computational experiments”. In: *Technometrics* 33.2 (1991), pp. 161–174.

[161] Andrea Saltelli and Paola Annoni. “How to avoid a perfunctory sensitivity analysis”. In: *Environmental Modelling & Software* 25.12 (2010), pp. 1508–1517.

[162] Andrea Saltelli, Stefano Tarantola, and K. S. Chan. “A quantitative model-independent method for global sensitivity analysis of model output”. In: *Technometrics* 41.1 (1999), pp. 39–56. DOI: 10.1080/00401706.1999.10485594.

[163] Koen Schepers, Timothy B Campbell, and Emmanuelle Passegué. “Normal and leukemic stem cell niches: insights and therapeutic opportunities”. In: *Cell stem cell* 16.3 (2015), pp. 254–267.

[164] Ilya M. Sobol. "Global sensitivity indices for nonlinear mathematical models and their Monte Carlo estimates". In: *Mathematics and Computers in Simulation* 55.1–3 (2001), pp. 271–280. DOI: 10.1016/S0378-4754(00)00270-6.
[165] Robert I. Cukier et al. "Study of the sensitivity of coupled reaction systems to uncertainties in rate coefficients. I. Theory". In: *The Journal of Chemical Physics* 59.8 (1973), pp. 3873–3878. DOI: 10.1063/1.1680571.
[166] Bruno Sudret. "Global sensitivity analysis using polynomial chaos expansions". In: *Reliability Engineering & System Safety* 93.7 (2008), pp. 964–979. DOI: 10.1016/j.ress.2007.04.002.
[167] Saman Razavi and Hoshin V. Gupta. "A new framework for comprehensive, robust, and efficient global sensitivity analysis: 1. Theory". In: *Water Resources Research* 52.1 (2016), pp. 423–439. DOI: 10.1002/2015WR017558.
[168] Andrea Saltelli, TH Andres, and T Homma. "Sensitivity analysis of model output: An investigation of new techniques". In: *Computational statistics & data analysis* 15.2 (1993), pp. 211–238.
[169] Andrea Saltelli, Stefano Tarantola, and Francesca Campolongo. "Sensitivity analysis as an ingredient of modeling". In: *Statistical science* (2000), pp. 377–395.
[170] E Borgonovo and L Peccati. "Uncertainty and global sensitivity analysis in the evaluation of investment projects". In: *International Journal of Production Economics* 104.1 (2006), pp. 62–73.
[171] VARS-TOOL Developers. *VARS-TOOL: Variogram Analysis of Response Surfaces (VARS) Toolbox*. https://github.com/vars-tool/vars-tool. GitHub repository, accessed 2026-02-09. 2026.
[172] Karen Chan, Andrea Saltelli, and Stefano Tarantola. "Sensitivity analysis of model output: variance-based methods make the difference". In: *Proceedings of the 29th conference on Winter simulation*. 1997, pp. 261–268.
[173] Ivano Azzini, Thierry A Mara, and Rossana Rosati. "Comparison of two sets of Monte Carlo estimators of Sobolindices". In: *Environmental Modelling & Software* 144 (2021), p. 105167.
[174] Andrea Saltelli et al. "Variance based sensitivity analysis of model output. Design and estimator for the total sensitivity index". In: *Computer physics communications* 181.2 (2010), pp. 259–270.
[175] Emanuele Borgonovo et al. "Global sensitivity analysis with mixtures: a generalized functional ANOVA approach". In: *Risk Analysis* 42.2 (2022), pp. 304–333.
[176] Thierry Crestaux, Olivier Le Matre, and Jean-Marc Martinez. "Polynomial chaos expansion for sensitivity analysis". In: *Reliability Engineering & System Safety* 94.7 (2009), pp. 1161–1172.
[177] Andrea Saltelli. "Making best use of model evaluations to compute sensitivity indices". In: *Computer physics communications* 145.2 (2002), pp. 280–297.
[178] Maxime Lenormand, Franck Jabot, and Guillaume Deffuant. "Adaptive approximate Bayesian computation for complex models". In: *Computational Statistics* 28.6 (2013), pp. 2777–2796.
[179] Olivier Cappé et al. "Population Monte Carlo". In: *Journal of Computational and Graphical Statistics* 13.4 (2004), pp. 907–929. DOI: 10.1198/106186004X12803. URL: https://doi.org/10.1198/106186004X12803.
[180] Wouter Huberts et al. "Applicability of the polynomial chaos expansion method for personalization of a cardiovascular pulse wave propagation model". In: *International*

journal for numerical methods in biomedical engineering 30.12 (2014), pp. 1679–1704.

[181] Gabriel N Mannis et al. "Phase 2 Multi-Arm Study of Magrolimab Combinations in Patients With Acute Myeloid Leukaemia". In: *EJHaem* 6.3 (2025), e70051.

[182] Miroslawa Siatecka and James J Bieker. "The multifunctional role of EKLF/KLF1 during erythropoiesis". In: *Blood, The Journal of the American Society of Hematology* 118.8 (2011), pp. 2044–2054.

[183] Tatsiana Ripich and Rolf Jessberger. "SWAP-70 regulates erythropoiesis by controlling α4 integrin". In: *Haematologica* 96.12 (2011), p. 1743.

[184] Hong Ye and Tracey A. Rouault. "Erythropoiesis and iron sulfur cluster biogenesis". In: *Advances in Hematology* 2010 (2010), p. 329394. DOI: 10.1155/2010/329394.

[185] Sandra Pinho and Paul S. Frenette. "Haematopoietic stem cell activity and interactions with the niche". In: *Nature Reviews Molecular Cell Biology* 20.5 (2019), pp. 303–320.

Appendix: Additional Figures and Analyses

Here we provide supplementary results not included in the main text.

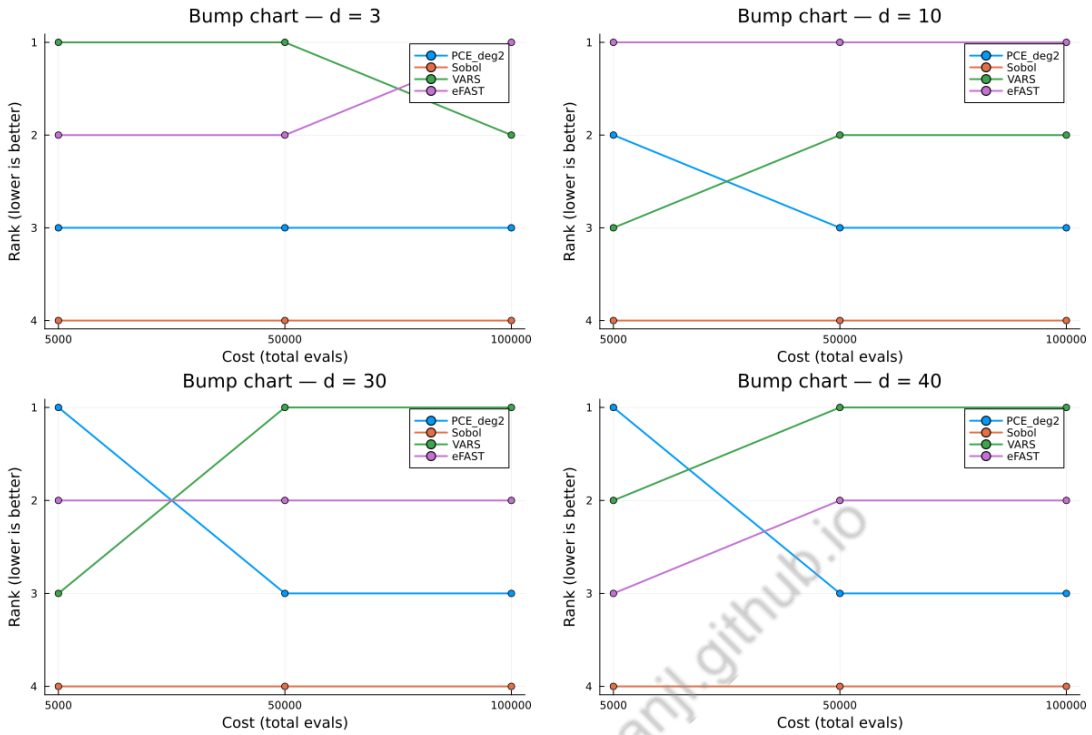

Figure 6.1: Bump charts showing method rankings by mean absolute error (lower rank = better) across matched computational budgets ($N = 5000, 50\,000, 100\,000$) for the Sobol–G function. (**Top left**) $d = 3$: VARS and eFAST achieve best ranks, while PCE remains stable and Sobol ranks lowest. (**Top right**) $d = 10$: eFAST leads consistently, VARS improves with cost, and PCE lags behind. (**Bottom left**) $d = 30$: VARS overtakes PCE at higher cost, eFAST holds intermediate performance. (**Bottom right**) $d = 40$: eFAST dominates at low cost, but VARS surpasses it as budget increases, while Sobol remains lowest ranked across all cases. These visualizations complement the error and gap plots in Section 3.4.1 by summarising relative method performance as rankings rather than absolute error values.

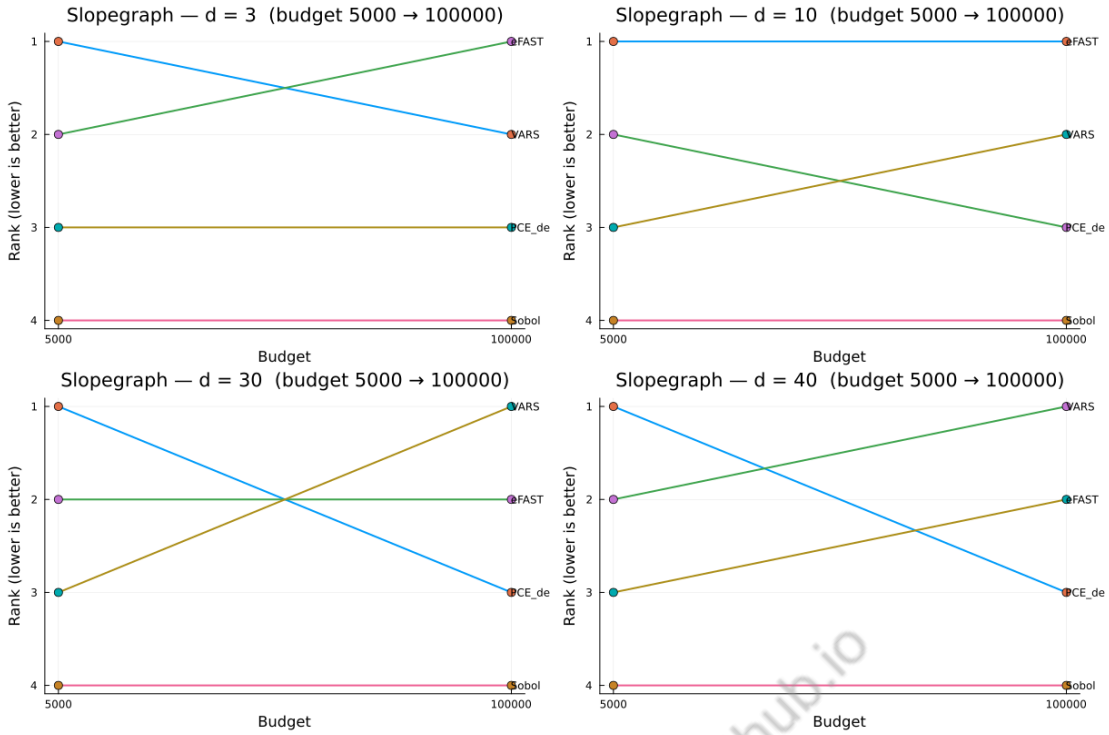

Figure 6.2: Slopegraphs showing method rankings by mean absolute error (lower rank = better) between the smallest ($N = 5000$) and largest ($N = 100\,000$) computational budgets for the Sobol–G benchmark at different dimensionalities. (**Top left**) $d = 3$: eFAST leads at low cost, but VARS improves and reaches second place. (**Top right**) $d = 10$: eFAST remains best ranked, with VARS improving relative to PCE. (**Bottom left**) $d = 30$: VARS rises to first place, while PCE drops in rank at higher budget. (**Bottom right**) $d = 40$: VARS surpasses all other methods, highlighting its robustness in high-dimensional settings, whereas Sobol remains consistently lowest ranked. These slopegraphs complement the bump charts (Figure 6.1) by emphasizing how rankings shift between minimum and maximum sample sizes.

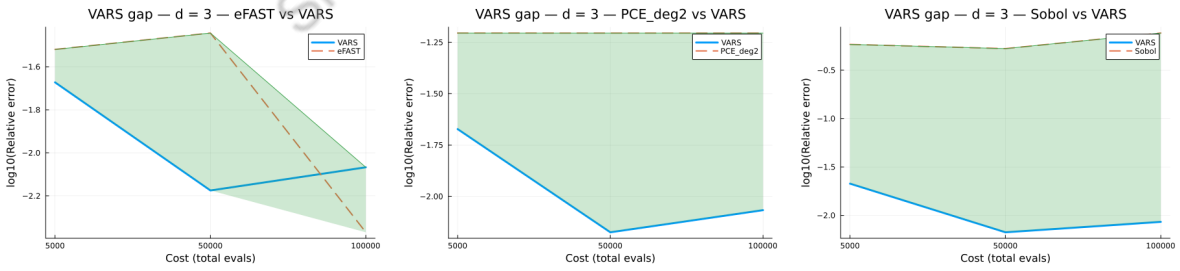

Figure 6.3: VARS gap plots for the Sobol–G benchmark at $d = 3$, comparing the relative error ($\log_{10}$ scale) of VARS against alternative methods across computational budgets ($N = 5000, 50\,000, 100\,000$ evaluations). (**Left**) VARS vs eFAST: both methods converge with increasing budget, with eFAST slightly more accurate. (**Middle**) VARS vs PCE: PCE maintains consistently lower error, highlighting its surrogate-based advantage in smooth, low-dimensional settings. (**Right**) VARS vs Sobol: VARS outperforms Sobol substantially, confirming its efficiency over variance-decomposition approaches under small budgets.

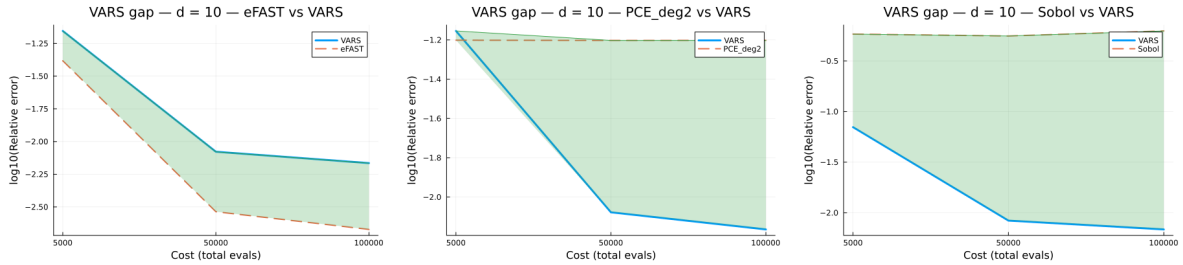

Figure 6.4: VARS gap plots for the Sobol–G benchmark at $d = 10$, comparing relative error ($\log_{10}$ scale) of VARS against other methods across budgets ($N = 5000, 50\,000, 100\,000$ evaluations). (**Left**) VARS vs eFAST: both methods achieve low error, with eFAST slightly ahead as dimension increases. (**Middle**) VARS vs PCE: PCE maintains lower error due to its surrogate expansion, while VARS converges steadily with more samples. (**Right**) VARS vs Sobol: VARS clearly outperforms Sobol, showing more than an order of magnitude lower error at high budgets.

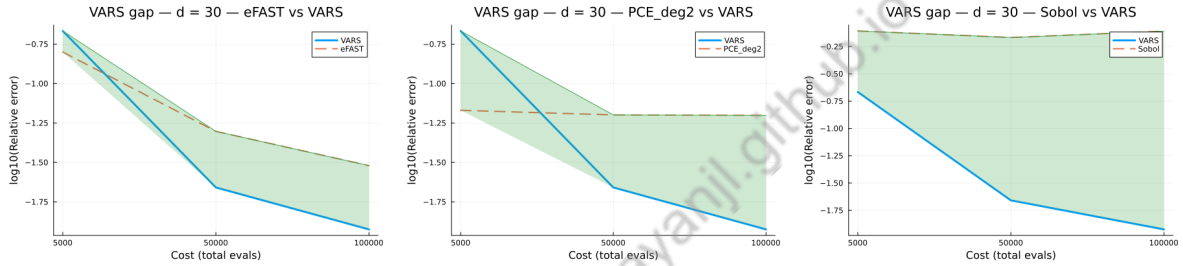

Figure 6.5: VARS gap plots for the Sobol–G benchmark at $d = 30$, comparing relative error ($\log_{10}$ scale) of VARS against other methods across budgets ($N = 5000, 50\,000, 100\,000$ evaluations). (**Left**) VARS vs eFAST: both methods converge steadily, with similar performance at high budgets. (**Middle**) VARS vs PCE: PCE retains lower error, but VARS narrows the gap with larger samples. (**Right**) VARS vs Sobol: VARS strongly outperforms Sobol, reducing error by more than an order of magnitude, especially at higher budgets.

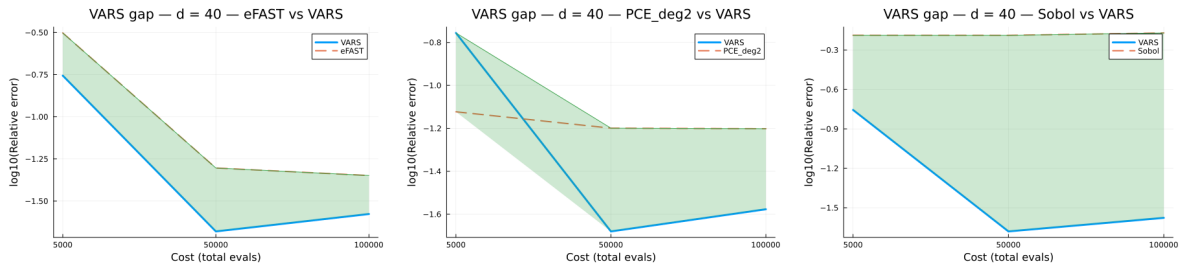

Figure 6.6: VARS gap plots for the Sobol–G benchmark at $d = 40$, comparing relative error ($\log_{10}$ scale) of VARS against alternative methods across computational budgets ($N = 5000, 50\,000, 100\,000$ evaluations). (**Left**) VARS vs eFAST: both methods converge, with eFAST slightly more accurate at higher budgets. (**Middle**) VARS vs PCE: PCE maintains lower error overall, but VARS narrows the gap as budget increases. (**Right**) VARS vs Sobol: VARS clearly outperforms Sobol, maintaining substantially lower error even in high-dimensional settings.